Multi-polarization scattering model induced by acoustic-elastic analogy for customized versatility of elastic meta-atoms

Yu-Ze Tian,[1] Yi-Ming Cui,[1] Li-Yun Cao,[1] Yan-Feng Wang,[1,2,*] Vincent Laude,[3] and Yue-Sheng Wang[1,4]

[1] *School of Mechanical Engineering, Tianjin University, 300350 Tianjin, China*
[2] *National Key Laboratory of Vehicle Power System, 300350 Tianjin, China*
[3] *Université Marie et Louis Pasteur, CNRS, Institut FEMTO-ST, F-25000 Besançon, France*
[4] *Institute of Engineering Mechanics, Beijing Jiaotong University, Beijing 100044, China*

Elastic waves propagating in thin plates provide sophisticated versatility for high-efficiency non-destructive testing and precise ultrasonic diagnostics, owing to their inherent complex polarization mixing in-plane displacements. However, versatility remains a challenge, due to the difficulty of simultaneously manipulating polarization components and customizing conversion between them. In this paper, the multimode scattering characteristics of a meta-atom for elastic waves under the plane stress approximation is systematically analyzed in view of the design of versatile devices. An acoustic-elastic analogy is first employed to describe the impedance and scattering matrices of the meta-atom. A 4-port model for in-plane multimode manipulation under normal incidence is then proposed. The construction naturally offers at least two different channels supporting two linearly independent functions. An elastic meta-atom containing a compression-torsion coupling structure is designed for complete mode conversion in both transmission and reflection. Extending the analysis to oblique incidence, an 8-port model with four internal channels is developed. By enhancing the asymmetry of the compression–torsion coupling meta-atom, four functions are integrated into the meta-atom. Extremely asymmetric scattering in 2D is demonstrated by a meta-atom array implementing Willis coupling. The versatility of designed meta-atoms are validated both by numerical simulations and experiments. The work in this paper may open up alternative perspectives on asymmetric wave manipulation and contributes to versatile elastic metamaterials design.

Keywords: Versatile metasurfaces; Elastic wave; Asymmetric scattering; Elastic meta-atom; Multimode manipulation

I. INTRODUCTION

The manipulation of elastic waves is garnering increasing attention due to their intrinsic multi-polarization capability[1–6]. Encompassing diverse behaviours and manipulating waves with different polarizations play a pivotal role in numerous modern engineering applications[7–9]. Comparing the polarization contrast between incident and reflected waves, internal structural cracks can be evaluated holographically without damage[10]. This ability facilitates the use of elastic waves as one of the primary means for structural health monitoring[11] and non-destructive testing[12]. Converting conventional pressure wave[13, 14] into transverse waves on the surface of skin or skull[15], shear ultrasound technique achieves superior imaging resolution in holographic systems[16]. This technique allows for detailed evaluation through the examination of the responses with varying polarizations[17], which furnishes a improved information capacity for diagnostics. However, implementation via active devises always faces inherent limitations, particularly high fabrication costs and complex control circuitry[18]. Designing passive structures for polarization customization has thus long been a significant challenge.

Metamaterials[19, 20] and metasurfaces[21] are widely recognized as revolutionary candidates for wave manipulation. They were initially proposed in acoustics for wave manipulation using passive structures with tailored dispersion properties[22–26]. Several methodologies have been established to guide structural design, including transformation theory[27–32], the generalized Snell's law[33–38], diffractive metagrating[39–42] and impedance theory[43–48]. They have enabled the development of distinct functions, ranging from invisibility cloaks[49–52], energy harvesting[53–57] and signal processing[58–63] to holographic imaging[64–68]. Given the shared time-harmonic wave propagation features between elastic and acoustic wave[69], these methodologies maintain complete functionality in elasticity[70–80]. Meanwhile, the multipolarized nature of elastic waves drives heated studies into polarization conversion. A solution for converting incident longitudinal waves to reflected transverse waves was first proposed with a metamaterial composed of staggered slits[81]. This structure was then topologically optimized to customize the propagating direction of the converted wave[82]. Another compact strategy is provided with a reflective metasurface tailored with extreme horizontal phase difference[83]. The metasurface can then support conversion from longitudinal to transverse waves

* wangyanfeng@tju.edu.cn

with a certain transmission angle. Based on the same idea but considering different structures, a refractive metasurface consisting of parallel-resonator units was proposed as well[84]. Broad-angle longitudinal-transverse wave conversion was achieved and validated in experiments.

Furthermore, the presence of vector variables in the elastic governing equation also enables the integration of multiple functions within elastic metasurfaces[85, 86]. The parallel-resonator unit was improved by completely controlling the transmission of either longitudinal or transverse waves while blocking the other[87]. The composed metasurface provides steering of specific waves selectively. Similarly, inspired by pentamode metamaterials regulating longitudinal waves separately, the concept of shear-wave metamaterials was proposed[88]. Refining it into a metasurface, full transmission of transverse waves can be realized while building a barrier for longitudinal waves. Superimposing mode conversion on these unidirectional metasurfaces, a quasi diode can be achieved[89, 90]. Longitudinal waves can be converted into transverse waves from one side but blocked from another. Contrarily, it was shown that a sophisticated metamaterial designed with specific anisotropy can achieve complete conversion between longitudinal and transverse waves from both sides[91]. It was then improved by integrating bidirectional mode conversion in rotationally symmetric metasurfaces at the sub-wavelength scale[92]. However, the underlying driving mechanism of multiple functions and the physical limits on simultaneous functions availability in an elastic-wave manipulation devices remain unclear and demand further systematic investigation. It was recently proven that acoustic metasurfaces can be tailored with multiple functions in selectively transmitting or reflecting obliquely incident waves[93]. Paralogically, double versatility with customized polarization conversion could be achieved by a elastic system through analogous design paradigms.

In this paper, a multi-polarization scattering model for customized versatility of elastic meta-atoms is proposed inspired by an acoustic-elastic analogy. Each meta-atom can be naturally represented by a 4-port scattering model with two linearly independent functions of in-plane mode manipulation under normal incidence. A sextuple compression-torsion coupling structure is proposed to implement the meta-atom. It exhibits significant versatility over transmission, reflection, and conversion between modes with different polarizations. By invoking Snell's law, the port count is increased to 8 when considering oblique incidence, enabling four linearly independent functions. For customization of asymmetric scattering, the meta-atom geometry is deliberately rendered asymmetric, referring to Willis metamaterials. Extreme asymmetry along both horizontal and vertical directions is achieved in transmission and in modal conversion of elastic waves. The designed meta-atoms are validated by numerical simulations and are experimentally characterized using a laser vibrometer. This work is expected to advance versatile elastic metamaterials and metasurfaces and to offer new design paradigms for their unit cells.

II. ACOUSTIC-ELASTIC ANALOGY

In this section, the acoustic-elastic analogy is established by comparing the governing equations of acoustic and elastic waves. The vector decomposition is introduced to decouple the vectorial variables in the Lamé-Navier equation. The induced quantities are defined accordingly to lead to a effective analogy between acoustics and elasticity under plane stress assumption.

Elastic waves are widely recognized to behave similarly to sound waves due to their similar governing equations. The time-harmonic governing equation for acoustic waves generally takes a Helmholtz form as

$$\nabla \cdot \left(\frac{1}{\rho} \nabla p \right) = -\frac{\omega^2}{K} p, \tag{1}$$

where p is the pressure field, ρ is the mass density, ω is the operating angular frequency and K is the bulk modulus. The propagation of elastic waves is determined by the harmonic Lamé-Navier equation

$$\left(\hat{\lambda} + 2\hat{\mu} \right) \nabla \left(\nabla \cdot \mathbf{u} \right) - \hat{\mu} \nabla \times \left(\nabla \times \mathbf{u} \right) = -\omega^2 \rho \mathbf{u}, \tag{2}$$

where $\hat{\lambda} = \frac{1-2\nu}{(1-\nu)}\lambda$ and $\hat{\mu} = \mu$ are the Lamé constants under the assumption of plane stress, ρ is the mass density. Here, the displacement vector is limited to in-plane components and is defined as $\mathbf{u} = (u, v)$. Hence we specifically assume that elastic waves propagate within the plane of a thin plate, which is a major operating condition for applications[94].

A vector decomposition is next introduced in order to decouple the variables in Eq. (2) and thus to establish an analogy between acoustics and elasticity. The divergence and the curl of the displacement vector are examined

$$\begin{aligned} \Phi &= \tfrac{\partial u}{\partial x} + \tfrac{\partial v}{\partial y}, \\ \Psi &= \tfrac{\partial v}{\partial x} - \tfrac{\partial u}{\partial y}. \end{aligned} \tag{3}$$

Changing variables in Eq. (2) and assuming propagation in a homogeneous thin plate, the governing equations can be expressed in a decoupled form as

$$\begin{aligned} \nabla\cdot\left(\tfrac{1}{\rho}\nabla P\right) &= -\omega^2\tfrac{1}{\hat{M}}P, \quad \text{where} \quad P=\hat{M}\Phi, \\ \nabla\cdot\left(\tfrac{1}{\rho}\nabla Q\right) &= -\omega^2\tfrac{1}{\hat{G}}Q, \quad \text{where} \quad Q=\hat{G}\Psi. \end{aligned} \tag{4}$$

where $\hat{M}=\hat{\lambda}+2\hat{\mu}$ and $\hat{G}=\hat{\mu}$ are the longitudinal and transverse wave modulii, respectively. Owing to the effective acoustic-elastic analogy, the physical meaning of induced quantities, including local velocity, intensity, and characteristic impedance, is preserved. These quantities read for acoustic waves

$$\mathbf{v}_p=\frac{\imath}{\omega\rho}\nabla p, \quad \mathbf{I}_p=\frac{1}{2}\mathrm{Re}\left[p\mathbf{v}_p^*\right], \quad Z_p=\frac{p}{|\mathbf{v}_p|}. \tag{5}$$

where $\imath$ is the imaginary unit and * represents conjugation. Therefore, the induced quantities for P and Q can be defined accordingly as

$$\begin{aligned} \mathbf{v}_P &= \tfrac{\imath}{\omega\rho}\nabla P, \ \mathbf{I}_P=\tfrac{1}{2}\mathrm{Re}\left[P\mathbf{v}_P^*\right], \ Z_P=\tfrac{P}{|\mathbf{v}_P|}, \\ \mathbf{v}_Q &= \tfrac{\imath}{\omega\rho}\nabla Q, \ \mathbf{I}_Q=\tfrac{1}{2}\mathrm{Re}\left[Q\mathbf{v}_Q^*\right], \ Z_Q=\tfrac{Q}{|\mathbf{v}_Q|}. \end{aligned} \tag{6}$$

All dependent variables now share the same dimensions, which leads to a direct analogy between acoustics (p) and plane stress elasticity (P and Q variables).

The 1D scattering of an acoustic or elastic meta-atom is therefore represented as port models in Fig. 1. Notably, all variables are normalized according to

$$\begin{aligned} \bar{p}&=\tfrac{p}{\sqrt{Z_p}}, \ \bar{\mathbf{v}}_p=\sqrt{Z_p}\mathbf{v}_p, \ \bar{\mathbf{I}}_p=\mathbf{I}_p=\tfrac{1}{2}\mathrm{Re}\left[\bar{p}\bar{\mathbf{v}}_p^*\right], \ \bar{Z}_p=\tfrac{\bar{p}}{\bar{\mathbf{v}}_p}=1, \\ \bar{P}&=\tfrac{P}{\sqrt{Z_P}}, \ \bar{\mathbf{v}}_P=\sqrt{Z_P}\mathbf{v}_P, \ \bar{\mathbf{I}}_P=\mathbf{I}_P=\tfrac{1}{2}\mathrm{Re}\left[\bar{P}\bar{\mathbf{v}}_P^*\right], \ \bar{Z}_P=\tfrac{\bar{P}}{\bar{\mathbf{v}}_P}=1, \\ \bar{Q}&=\tfrac{Q}{\sqrt{Z_Q}}, \ \bar{\mathbf{v}}_Q=\sqrt{Z_Q}\mathbf{v}_Q, \ \bar{\mathbf{I}}_Q=\mathbf{I}_Q=\tfrac{1}{2}\mathrm{Re}\left[\bar{Q}\bar{\mathbf{v}}_Q^*\right], \ \bar{Z}_Q=\tfrac{\bar{Q}}{\bar{\mathbf{v}}_Q}=1. \end{aligned} \tag{7}$$

They now share a dimensionless unit characteristic impedance leading to a unitary scattering matrix[48].

III. 4-PORT SCATTERING MODEL AND COMPRESSION-TORSION COUPLED META-ATOM

In this section, a 4-port scattering model is developed for the elastic meta-atom. A compression-torsion coupled structure is designed for the implementation of the scattering customization. Its scattering matrix is analyzed and verified by measuring the port response under two linearly independent excitations.

An acoustic meta-atom can be described by a 2-port model as shown in Fig. 1(a). For a given input $\left(\bar{p}_1^{\mathrm{in}},\bar{p}_2^{\mathrm{in}}\right)^{\mathrm{T}}$, its output $\left(\bar{p}_1^{\mathrm{out}},\bar{p}_2^{\mathrm{out}}\right)^{\mathrm{T}}$ is determined by

$$\begin{bmatrix}\bar{p}_1^{\mathrm{out}}\\ \bar{p}_2^{\mathrm{out}}\end{bmatrix}=\mathbf{S}\begin{bmatrix}\bar{p}_1^{\mathrm{in}}\\ \bar{p}_2^{\mathrm{in}}\end{bmatrix}. \tag{8}$$

where $\mathbf{S}$ is the second-order scattering matrix

$$\mathbf{S}=\begin{bmatrix}S_{11} & S_{12}\\ S_{21} & S_{22}\end{bmatrix}. \tag{9}$$

For a linear and conservative system, the scattering matrix is symmetrc and unitary

$$\mathbf{S}=\mathbf{S}^{\mathrm{T}}, \tag{10}$$

$$\mathbf{S}\mathbf{S}^{\mathrm{H}}=\mathbf{E}, \tag{11}$$

where T and H denote transposition and conjugate transposition,respectively, and $\mathbf{E}$ is the identity matrix. One can retrieve a column of the scattering matrix by measuring at the two output ports under the excitation on one input port[95]. The other components are then determined by the symmetry condition Eq.(10) and the unitary condition Eq.(11). This way the complete scattering characteristics of the meta-atom, i.e. all components in its

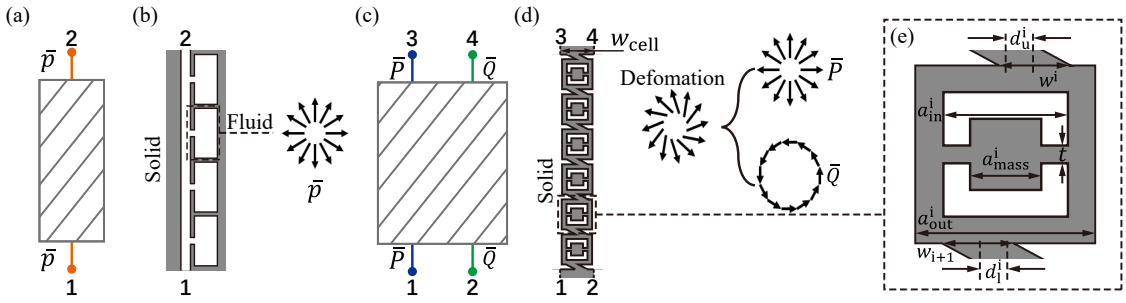

FIG. 1. 1D scattering model and structure design of an acoustic or elastic meta-atom. (a) 2-port model for acoustic meta-atom. (b) Quadruple Helmholtz resonance structure. (c) 4-port model for elastic meta-atom. (d) Elastic sextuple compression-torsion coupled structure. (e) Geometric parameter settings for optimization.

scattering matrix, are obtained[96]. Naturally, there should be only one channel inside the meta-atom, connecting port 1 and port 2 directly. It is generally believed that the quadruple Helmholtz resonance structure shown in Fig. 1(b) is suitable for acoustic scattering customization[97]. Each substructure incorporates a resonant cavity and a neck, providing inertia and stiffness, respectively. The interior of the cavity sustains deformations of the fluid – expansion and compression – but no shearing.

Things become completely different for an elastic meta-atom with two different dependent variables. According to the analogy established by Eq. (8), the meta-atom can be regarded as a 4-port system, as shown in Fig. 1 (c). The relationship between input ports and output ports is determined by the scattering matrix

$$\begin{bmatrix} \bar{P}_1^{\text{out}} \\ \bar{Q}_2^{\text{out}} \\ \bar{P}_3^{\text{out}} \\ \bar{Q}_4^{\text{out}} \end{bmatrix} = \begin{bmatrix} S_{11} & S_{12} & S_{13} & S_{14} \\ S_{21} & S_{22} & S_{23} & S_{24} \\ S_{31} & S_{32} & S_{33} & S_{34} \\ S_{41} & S_{42} & S_{43} & S_{44} \end{bmatrix} \begin{bmatrix} \bar{P}_1^{\text{in}} \\ \bar{Q}_2^{\text{in}} \\ \bar{P}_3^{\text{in}} \\ \bar{Q}_4^{\text{in}} \end{bmatrix}. \tag{12}$$

This scattering matrix is of fourth-order but is still symmetric [Eq.(10)] and unitary [Eq.(11)] as long as the meta-atom is linear and conservative. Owing to these two properties, the complete scattering characteristics can be obtained from two linearly independent excitations. Two columns of the scattering matrix can be obtained by measuring at the ports. The other components can be calculated from the symmetry and unitary conditions. Therefore, the meta-atom is anticipated to provide two linearly independent internal channels corresponding to two inherent functions. However, it should be mentioned that the scattering matrix cannot be fully determined if the two excitations are correlated. For example, one may easily design a meta-atom to provide simple full transmission to both longitudinal and transverse waves without mode conversion[86]. The arrangement of channels within the meta-atom is shown in Fig. 1(c). The scattering matrix cannot be read completely when exciting it by two longitudinal waves incident on ports 1 and 3. Only one channel is excited, whereas the other channel remains untested.

According to the acoustic-elastic analogy, a compression-torsion coupled structure is designed for the implementation of the meta-atom as shown in Fig. 1(d). In consideration that $\bar{p}$ and $\bar{P}$ share the same deformation mode, the structure should be able to provide expansion and compression. $\bar{Q}$ then determines that the structure should carry torsional deformation as well. Consequently, each substructure is designed to comprise a mass block enclosed by a rectangular shell, while adjacent substructures are interconnected via inclined strips. Six substructures connected in series constitute one meta-atom in this paper. The mass block and the rectangular shell contribute to inertia stiffness, respectively, for expansion and compression. Meanwhile, the mass block and the inclined strip also contribute to rotational inertia and rotational stiffness, respectively. Notably, as a resonant structure, the effective mass density and effective stiffness are allowed to be negative for both $\bar{P}$ and $\bar{Q}$. It is expected that the propagation and the conversion of two different dependent variables can be covered simultaneously.

The assumption of homogeneity of the thin plate in Sect. II applies to the two external media surrounding a meta-atom, but is not necessary within it. Therefore, a simple model is presented next to assess the scattering performance of the meta-atom[85, 98, 99]. The wave behavior of the meta-atom depicted in Fig. 1 (d) under normal incidence can be described by a set of 1D equations

$$\frac{\partial}{\partial y}\begin{bmatrix} \frac{1}{\rho_P} & \frac{b}{\rho_0} \\ \frac{b}{\rho_0} & \frac{1}{\rho_Q} \end{bmatrix}\frac{\partial}{\partial y}\begin{bmatrix} P \\ Q \end{bmatrix} = -\omega^2 \begin{bmatrix} \frac{1}{\tilde{M}_m} & 0 \\ 0 & \frac{1}{\tilde{G}_m} \end{bmatrix}\begin{bmatrix} P \\ Q \end{bmatrix}, \tag{13}$$

where $\rho_P = a\rho_0$, $\rho_Q = c\rho_0$ and $\hat{M}_m = d\hat{M}_0$, $\hat{G}_m = e\hat{G}_0$ are the effective mass density and effective stiffness for P and Q inside the meta-atom, respectively, and b is the coupling strength between them. The induced local velocities are implicitly defined as

$$\begin{aligned} \mathbf{v}_P &= \frac{\imath}{\omega}\left(\frac{1}{\rho_P}\frac{\partial P}{\partial y} + \frac{b}{\rho_0}\frac{\partial Q}{\partial y}\right), \\ \mathbf{v}_Q &= \frac{\imath}{\omega}\left(\frac{b}{\rho_0}\frac{\partial P}{\partial y} + \frac{1}{\rho_Q}\frac{\partial Q}{\partial y}\right). \end{aligned} \tag{14}$$

To obtain a definite solution, the generalized eigenvalue problem is formulated as

$$\left(r\begin{bmatrix} \frac{1}{\rho_P} & \frac{b}{\rho_0} \\ \frac{b}{\rho_0} & \frac{1}{\rho_Q} \end{bmatrix} - \omega^2 \begin{bmatrix} \frac{1}{\hat{M}_m} & 0 \\ 0 & \frac{1}{\hat{G}_m} \end{bmatrix}\right) L = 0, \tag{15}$$

Then the characteristic equation is established as

$$\begin{vmatrix} \frac{r}{\rho_P} - \frac{\omega_0^2}{\hat{M}_m} & r\frac{b}{\rho_0} \\ r\frac{b}{\rho_0} & \frac{r}{\rho_Q} - \frac{\omega_0^2}{\hat{G}_m} \end{vmatrix} = 0. \tag{16}$$

The two eigenvalues are solved as

$$r_{1,2} = \omega_0^2 \frac{\frac{1}{\rho_Q \hat{M}_m} + \frac{1}{\rho_P \hat{G}_m} \pm \sqrt{\left(\frac{1}{\rho_Q \hat{M}_m} - \frac{1}{\rho_P \hat{G}_m}\right)^2 + 4\frac{b^2}{\rho_0^2}\frac{1}{\hat{M}_m}\hat{G}_m}}{2\left(\frac{1}{\rho_P \rho_Q} - \frac{b^2}{\rho_0^2}\right)}. \tag{17}$$

Substituting them into Eq. (15), the eigenvectors are

$$L_1 = \begin{bmatrix} r_1\frac{b}{\rho_0} \\ -\left(\frac{r_1}{\rho_P} - \frac{\omega_0^2}{\hat{M}_m}\right) \end{bmatrix} = \begin{bmatrix} m_1 \\ n_1 \end{bmatrix}, \qquad L_2 = \begin{bmatrix} r_2\frac{b}{\rho_0} \\ -\left(\frac{r_2}{\rho_P} - \frac{\omega_0^2}{\hat{M}_m}\right) \end{bmatrix} = \begin{bmatrix} m_2 \\ n_2 \end{bmatrix}. \tag{18}$$

Owing to linearity, the wavefield within the meta-atom always follows a form of the type

$$\begin{bmatrix} P \\ Q \end{bmatrix} = \alpha_1 e^{\imath\sqrt{r_1}y} L_1 + \alpha_2 e^{\imath\sqrt{r_2}y} L_2 + \alpha_3 e^{-\imath\sqrt{r_1}y} L_1 + \alpha_4 e^{-\imath\sqrt{r_2}y} L_2. \tag{19}$$

For a meta-atom placed between planes $y_1 = 0$ and $y_2 = h_0$, the impedance matrix is defined as

$$\begin{bmatrix} P|_1 \\ Q|_1 \\ P|_2 \\ Q|_2 \end{bmatrix} = \begin{bmatrix} Z_{11} & Z_{12} & Z_{13} & Z_{14} \\ Z_{21} & Z_{22} & Z_{23} & Z_{24} \\ Z_{31} & Z_{32} & Z_{33} & Z_{34} \\ Z_{41} & Z_{42} & Z_{43} & Z_{44} \end{bmatrix} \begin{bmatrix} -\mathbf{n}_1 \cdot \mathbf{v}_P|_1 \\ -\mathbf{n}_1 \cdot \mathbf{v}_Q|_1 \\ -\mathbf{n}_2 \cdot \mathbf{v}_P|_2 \\ -\mathbf{n}_2 \cdot \mathbf{v}_Q|_2 \end{bmatrix}, \tag{20}$$

where $\mathbf{n}_i$ is the the outward normal vector corresponding to y_i. Notably, the impedance matrix uniquely corresponds to the meta-atom itself, free of α. Therefore, its components can be obtained through the method of undetermined coefficients (details are provided in Appendix A). Connecting two identical homogeneous elastic thin plates with longitudinal wave modulus M_0, transverse wave modulus G_0, and mass density ρ_0 on both sides of the meta-atom, the normalized impedance matrix is defined as

$$\bar{Z} = \begin{bmatrix} \frac{1}{\sqrt{M_0\rho_0}} & 0 & 0 & 0 \\ 0 & \frac{1}{\sqrt{G_0\rho_0}} & 0 & 0 \\ 0 & 0 & \frac{1}{\sqrt{M_0\rho_0}} & 0 \\ 0 & 0 & 0 & \frac{1}{\sqrt{G_0\rho_0}} \end{bmatrix} \begin{bmatrix} Z_{11} & Z_{12} & Z_{13} & Z_{14} \\ Z_{21} & Z_{22} & Z_{23} & Z_{24} \\ Z_{31} & Z_{32} & Z_{33} & Z_{34} \\ Z_{41} & Z_{42} & Z_{43} & Z_{44} \end{bmatrix} \begin{bmatrix} \frac{1}{\sqrt{M_0\rho_0}} & 0 & 0 & 0 \\ 0 & \frac{1}{\sqrt{G_0\rho_0}} & 0 & 0 \\ 0 & 0 & \frac{1}{\sqrt{M_0\rho_0}} & 0 \\ 0 & 0 & 0 & \frac{1}{\sqrt{G_0\rho_0}} \end{bmatrix}, \tag{21}$$

Then the scattering matrix can be calculated by formula

$$\mathbf{S} = \left(\bar{\mathbf{Z}} + \mathbf{E}\right)\left(\bar{\mathbf{Z}} - \mathbf{E}\right)^{-1}. \tag{22}$$

A numerical model is presented in Fig. 1 (d) to estimate the performance of the proposed structure, which was implemented using the COMSOL Partial Differential Equation (PDE) module. The operating frequency is selected as $f_0 = 30$ kHz. The height of the meta-atom is set to $h_0 = 7.9$ cm and its width is set to $w_{\text{cell}} = 1.3$ cm. The background media on the upper and lower sides of the meta-atom are governed by Eq. (4) and are set to the same width as the meta-atom. They are made of aluminium, whose mass density is 2700 kg/m^3, plane stress longitudinal wave modulus is 77 GPa, and plane stress transverse wave modulus is 26 GPa. Then, the wavelength of longitudinal waves is $\lambda_P = 17.8$ cm, and the wavelength of transverse waves is $\lambda_P = 10.3$ cm. With respect to transverse waves, the height of meta-atom is at the sub-wavelength scale, while the tangential scale is at the deeply sub-wavelength scale. The length of the background media is set as $l_0 = 3\lambda_P$. The medium in the meta-atom is governed by Eq. (13). Periodic boundary conditions are set on the left and right boundaries of the model. The upper and lower ends are connected to perfectly matched layers with a thickness of $t_{\text{pml}} = \lambda_p$ to avoid spurious reflections (not drawn for simplicity). The Dirichlet boundary condition is set on the boundary of the PML as the excitation, with $P = 1$ or $Q = 1$

There are diverse connection configurations for the ports in Fig. 1 (c). Two cases of extreme modes manipulation of elastic waves are considered as examples. A transmission case of bidirectional mode conversion from longitudinal waves to transverse waves and conversely is examined first, as illustrated in Figs. 2(a). One channel connects port 1 to port 4 (yellow channel) and the other channel connects port 2 to port 3 (orange channel). The yellow channel should provide complete transmission, thus

$$|S_{14}^{\text{obj}}| = |S_{41}^{\text{obj}}| = 1. \tag{23}$$

Meanwhile, the transmittance of the orange channel should also be 100%, which leads to

$$|S_{23}^{\text{obj}}| = |S_{32}^{\text{obj}}| = 1. \tag{24}$$

Therefore, the amplitude of each component of its scattering matrix is expected to be

$$\text{abs}\left(\mathbf{S}^{\text{obj}}\right) = \begin{bmatrix} 0 & 0 & 0 & 1 \\ 0 & 0 & 1 & 0 \\ 0 & 1 & 0 & 0 \\ 1 & 0 & 0 & 0 \end{bmatrix}. \tag{25}$$

Combining Eqs. (22) and (25), the unknown parameters, i.e. the effective parameters of the meta-atom, are uniquely determined. Newton iteration is employed to provide a specific example (details are provided in Appendix B). The numerical responses of the effective-parameter meta-atom under all port excitations are shown in Fig. 2(b-e). The amplitude of all incident waves is set to unity. The excitation at port 1 implies the incidence of longitudinal ($\bar{P}$) waves from below as shown in Fig. 2(b). It can be noted that longitudinal waves are converted to transverse waves completely after passing through the meta-atom. This phenomenon exactly matches the yellow channel connecting port 1 and port 4. When the excitation is then placed at port 2, transverse waves ($\bar{Q}$) are incident from below as shown in Fig. 2(c). Perfect conversion to longitudinal waves propagating upwards is observed, which matches the orange channel connecting port 2 and port 3. Conversely, longitudinal waves incident from above are completely converted into transverse waves propagating downward as shown in Fig. 2(d). The fields in Fig. Fig. 2(c) and (d) are identical, because reciprocity is intrinsic to this linear and conservative system. The channel remains the same whether the meta-atom is excited at port 2 or at port 3. When the input power at port 2 is fully transmitted to port 3, the reciprocal response is obtained by exciting at port 3. Similarly, when the meta-atom is excited at port 4, as shown in Fig. 2(e), the response is same as Fig. 2(b).

A second case of channel connection for reflection bidirectional mode conversion is considered next, as shown in Fig. 2(f). One channel connects port 1 to port 2 (yellow channel), and the other channel connects port 3 to port 4 (orange channel). The orange channel should provide a complete transmission with

$$|S_{12}^{\text{obj}}| = |S_{21}^{\text{obj}}| = 1. \tag{26}$$

Similarly, the yellow channel should also provide a transmissivity of 100%, i.e.

$$|S_{34}^{\text{obj}}| = |S_{43}^{\text{obj}}| = 1. \tag{27}$$

The amplitudes of each component of the scattering matrix are determined as

$$\text{abs}\left(\mathbf{S}^{\text{obj}}\right) = \begin{bmatrix} 0 & 1 & 0 & 0 \\ 1 & 0 & 0 & 0 \\ 0 & 0 & 0 & 1 \\ 0 & 0 & 1 & 0 \end{bmatrix}. \tag{28}$$

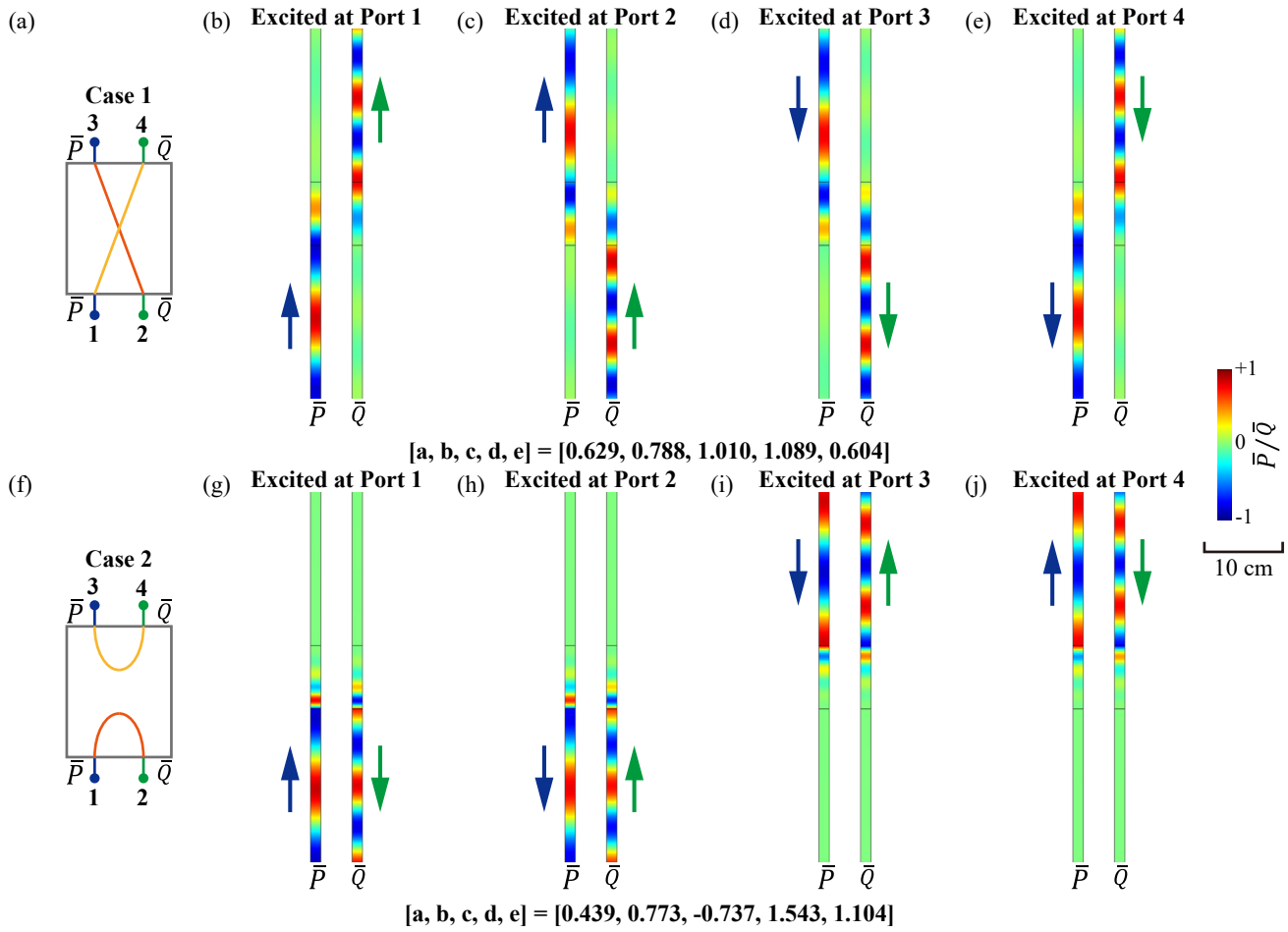

FIG. 2. The responses of the effective-parameter meta-atom for transmission and reflection bidirectional mode conversion. (a) 4-port model for transmission bidirectional mode conversion. (b) The response of the meta-atom under longitudinal waves incident from the lower side, i.e. excited at port 1. (c) The response of the meta-atom under transverse waves incident from the lower side, i.e. excited at port 2. (d) The response of the meta-atom under longitudinal waves incident from the upper side, i.e. excited at port 3. (e) The response of the meta-atom under transverse waves incident from the upper side, i.e. excited at port 4. (f) 4-port model for reflection bidirectional mode conversion. (g) The response of the meta-atom under longitudinal waveq incident from the lower side, i.e. excited at port 1. (h) The response of the meta-atom under transverse waves incident from the lower side, i.e. excited at port 2. (i) The response of the meta-atom under longitudinal waves incident from the upper side, i.e. excited at port 3. (j) The response of the meta-atom under transverse waves incident from the upper side, i.e. excited at port 4.

With the help of Newton iteration, the responses of the effective-parameter meta-atom under different excitations are depicted in Fig. 2(g-j). It can be noticed that longitudinal waves incident from below are reflected backward but are converted to transverse waves, as shown in Fig. 2(g). Due to the natural reciprocity explained earlier, transverse waves incident from the lower side are also completely reflected in the form of longitudinal waves, as shown in Fig. 2(h). Similarly, longitudinal waves incident from above are reflected into transverse waves, and vice versa, as shown in Fig. 2(i) and (j).

Parameter optimization is next conducted to provide practicable structures for the meta-atom. It is established in the COMSOL Multiphysics Solid Mechanics module cooperating with Matlab. The background medium and settings are the same as above, but replacing the effective-parameter meta-atom with the actual structures in Fig. 1 (d). Each compression-torsion coupling substructure, as shown in Fig. 1 (e), occupies a square area of 1.2 cm $\times$ 1.2 cm. Then, there could be at least a gap of $\delta/2 = 0.05$ cm at each side of the meta-atom for isolation. The outer side length of the square frame of the i-th substructure from top to bottom is a^i_{out}, and its inner side length is a^i_{in}. The side length of the mass block in the center of the frame is a^i_{mass}. The thickness of the strip connecting the mass block and the frame is $t = 0.1$cm. The width of the i-th inclined strip connecting the frames is w_i. The distances from

the center of the inclined strip connection at the top and bottom of the i-th substructure to the central axis of the meta-atom are d_{u}^{i} and d_{l}^{i}, respectively. The first and last strips are connected to the background medium on both sides. To ensure that the meta-atom and the background media on both sides are coaxial, we set the midpoint of the two connections to coincide with the central axis of the meta-atom. For the purpose of fabrication with the laser cutting technique, all corners are chamfered with a radius of $r = 0.02$ mm. Then, parameter optimization for structure design is implemented based on a genetic algorithm including 37 parameters. Two columns of scattering matrix can be obtained by extracting the longitudinal and transverse wave fields on both sides of the meta-atom (see Appendix C for a detailed retrieval procedure for the scattering matrix). It should be mentioned that two linearly independent excitations need to be examined in optimization (detailed simulation settings are recorded in Appendix D). Then, the other components are determined by Eqs. (10) and (11).

In order to perform parameter optimization for the meta-atom in Case 1, the fitness function is defined as the minimum value of the transmittance of the target channel. For the meta-atom in Case 1, it is set as

$$f = \min\left\{|S_{14}|, |S_{41}|, |S_{23}|, |S_{32}|\right\}. \tag{29}$$

The detailed optimization results is recorded in the second column of Table I and the corresponding amplitudes of each component of the scattering matrix are recorded in the second column of Table II. Numerical simulations for the response of the optimized meta-atom under the incidence of longitudinal and transverse waves from both sides are given in Fig. 3(a-d). All amplitudes are normalized with respect to the amplitude of the incident wave. The response under the excitation at port 1 in Fig. 3(a) is almost the same as Fig. 2(b). Longitudinal waves are converted to transverse waves after passing through the structure. When the excitation is placed at port 2, the amplitude of the transmitted longitudinal waves in Fig. 3(b) and Fig. 2(c) are basically the same as well. Some differences can be noted in their phases, which is reasonable as the solution to Eq. (25) is not unique. Owing to reciprocity, the responses for excitation set at port 3 in Fig. 3(c) and port 4 in Fig. 3(d) are consistent with Figs. 3(b) and (a), respectively. It is worth noting that the vibration mode of the meta-atom is identical when examinating the same channel from different ports. It can also be concluded that the physical essence of each channel is actually a specific vibration mode (eigenmodes of the meta-atom are provided in Appendix E to reveal the physical essence behind this phenomenon).

The fitness function for the meta-atom in Case 2 is set to the minimum value of the non-zero components of the object scattering matrix

$$f = \min\left\{|S_{12}|, |S_{21}|, |S_{34}|, |S_{43}|\right\}. \tag{30}$$

The detailed optimization results is recorded in the third column of Table I. The amplitudes of each component of the scattering matrix are recorded in the third column of Table II. The responses of the optimized structure under different excitations are depicted in Fig. 3(e-h). When the meta-atom is excited at port 1 or port 2 respectively, its response is identical, as shown in Figs. 3(e) and (f). Incident waves from below are reflected with opposite polarizations, exhibiting only slight phase deviation from Figs. 2(g) and (h). The same observation holds for Figs. 3(g) and (h), where complete mode-conversion reflections are achieved on the upper side of the meta-atom. Similar to Case 1, the vibration modes within the meta-atom are identical as long as the same channel is excited.

Moreover, in order to illustrate the generality of the designed structure, three additional examples, including selective transmission (Case 3), unidirectional mode conversion (Case 4), and complete transmission (Case 5), are given in Appendix F.

For an intuitive illustration, the collective response of the designed bidirectional mode conversion meta-atom is given in Fig. 4 (the detailed settings of the simulations are recorded in Appendix D). Radiation patterns are also provided for quantitative evaluation with the incident wave as a reference. For the meta-atom of Case 1, it can be noted that longitudinal waves incident from below are converted into transverse waves after passing through the meta-atom array, as shown in Fig. 4(a), which corresponds to the channel connecting port 1 and 4. Parasitic scattering arises on both sides but remains minor, since the incident wave is not strictly plane. It can be noted that the main lobe of the converted transverse wave (green solid line) is longer and thinner than the main lobe of the incident longitudinal wave for reference (blue dashed line). This is introduced by the contrast in the wavelengths of transverse and longitudinal waves. Transverse waves with a shorter wavelength have relatively more concentrated power in the far field when the beam width is the same. Although the amplitudes of the lobes seem to be different, their total power is conserved. Meanwhile, transverse waves incident from below are also converted into transmitted longitudinal waves as shown in Fig. 4(b), which is related to the another channel connecting port 2 and 3. The amplitude of the converted longitudinal waves in the far field is lower than that of the transverse waves for the same reason, although the conversion efficiency is close to 100%. Due to the natural reciprocity of linear systems, the phenomena in Fig. 4(c) and (d) are consistent with Fig. 4(b) and (a), respectively.

For the meta-atom of Case 2, longitudinal and transverse waves incident from the lower side are converted to each other after reflection, as shown in Figs. 4(e) and (f), respectively. It can be observed from their radiation patterns

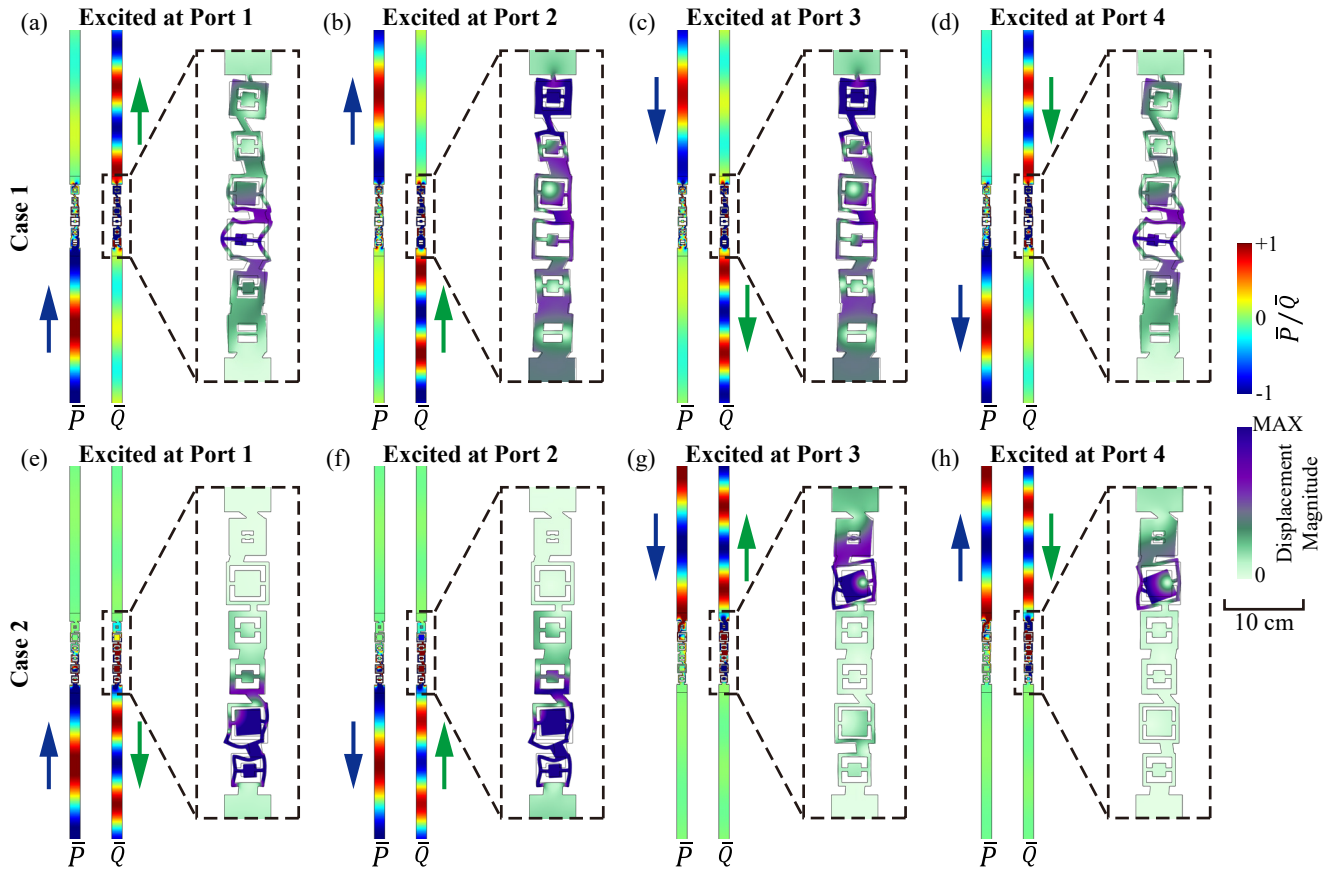

FIG. 3. Structure design of the meta-atom and responses for transmission and reflection bidirectional mode conversion. (a) The response of transmission meta-atom under longitudinal waves incident from the lower side, i.e. excited at port 1. (b) The response of transmission meta-atom under transverse waves incident from the lower side, i.e. excited at port 2. (c) The response of transmission meta-atom under longitudinal waves incident from the upper side, i.e. excited at port 3. (d) The response of transmission meta-atom under transverse waves incident from the upper side, i.e. excited at port 4. (e) The response of reflection meta-atom under longitudinal waves incident from the lower side, i.e. excited at port 1. (f) The response of reflection meta-atom under transverse waves incident from the lower side, i.e. excited at port 2. (g) The response of reflection meta-atom under longitudinal waves incident from the upper side, i.e. excited at port 3. (h) The response of reflection meta-atom under transverse waves incident from the upper side, i.e. excited at port 4.

that almost no unexpected scattering occurs. Their conversion rates are the same due to reciprocity and are close to 100%. Similarly, the phenomena for longitudinal and transverse waves incident from the upper side in Figs. 4(g) and (h) are the same, because of reciprocity again. Almost no waves can be detected in the transmitted field, which is consistent with the radiation pattern.

IV. 8-PORT MODEL FOR ELASTIC META-ATOM UNDER OBLIQUE INCIDENCE AND EXTREME ASYMMETRIC MULTI-MODE-DIRECTION SCATTERING

In this section, an 8-port model with an 8×8 scattering matrix is developed for multi-mode-direction scattering under oblique incidence. The scattering characteristics can be customized by connecting different input and output ports through internal channels. An asymmetric meta-atom design is proposed to achieve extreme asymmetric scattering of both mode perseveration and conversion simultaneously.

Things change a lot when waves are no longer incident along the normal direction. The oblique incidence model for a metasurface composed of a meta-atom array is depicted in Fig. 5(a). Following Snell's law, four waves would be excited under a wave longitudinal incident from the upper left (port 3) with an incidence angle of $\theta_{\bar{P}}$. There is a pair of longitudinal waves on the right hand side including one reflected (port 7) and one refracted (port 5). Their reflection angle and refraction angle are both $\theta_{\bar{P}}$. Meanwhile, a pair of transverse waves is excited as well, whose

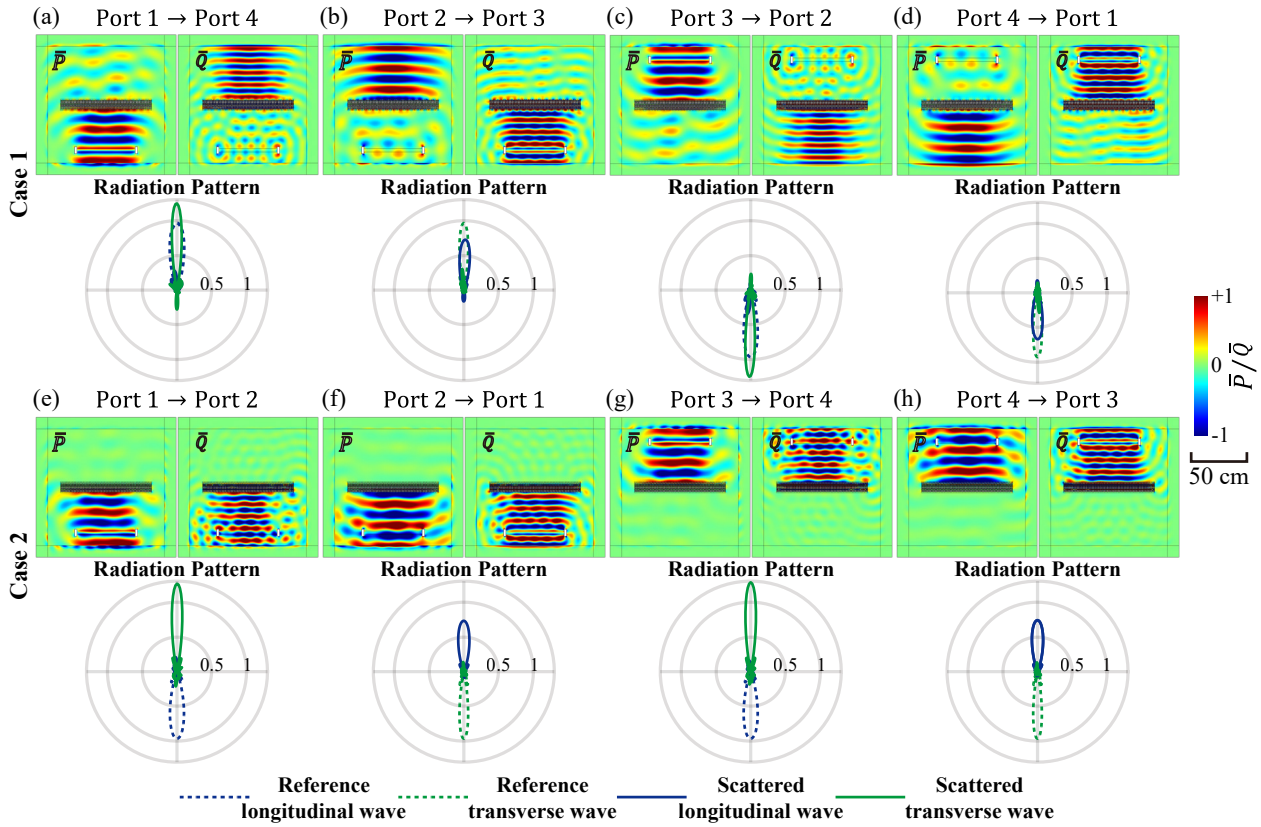

FIG. 4. Collective response of the designed bidirectional mode conversion meta-atom and corresponding radiation pattern. The transmission meta-atom of Case 1 under the excitation of (a) longitudinal wave incidence from the lower side, (b) transverse wave incidence from the lower side, (c) longitudinal wave incidence from the upper side, and (d) transverse wave incidence from the upper side. The reflection meta-atom of Case 2 under the excitation of (e) longitudinal wave incidence from the lower side, (f) transverse wave incidence from the lower side, (g) longitudinal wave incidence from the upper side, and (h) transverse wave incidence from the upper side.

reflection angle and refraction angle are both $\theta_{\bar{Q}}$ (ports 6 and 8). All angles obey Snell's law

$$k_{\bar{P}} \sin\theta_{\bar{P}} = k_{\bar{Q}} \sin\theta_{\bar{Q}}, \tag{31}$$

where $k_{\bar{P}}$ and $k_{\bar{Q}}$ are the wavenumbers of longitudinal and transverse waves, respectively. Similarly, transverse waves incident from the upper left side (port 4) or longitudinal and transverse waves incident from the lower left side (ports 1 or 2) would excites the same responses.

In the one-dimensional case, the scattering of the meta-atom can be fully described by a 4-port model, as analyzed in Section III. For a wave incident normally, such as a longitudinal wave at port 1, the reflected longitudinal wave shares the same port as the incident one. The transmission from all other ports (from port a) to this pair of longitudinal waves must be identical and equal to S_{a1}. However, when considering oblique incidence at port 1, the reflected wave with the same mode exhibits a symmetric reflection angle relative to the incident angle. Incident and reflected waves thus correspond to two different ports (port 1 and port 5). Transmission from all other ports (from port a) to the two ports is then different (S_{a1} and S_{a5}). Therefore, the 4-port model is no longer applicable to the case of oblique incidence. Numbering wave ports according to Fig. 5(a), an 8-port model is established for the description of the scattering characteristics of the meta-atom under oblique incidence, as shown in Fig. 5(b). The relationship between

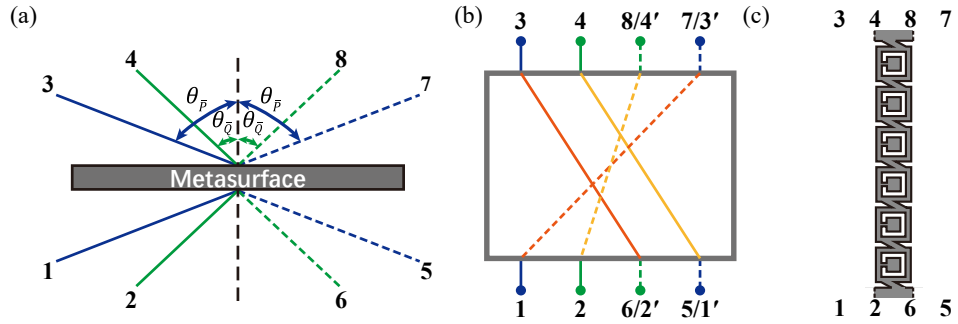

FIG. 5. Multi-scattering model for the elastic meta-atom. (a) A general scattering model for elasticity determined by Snell's law. (b) 8-port model for multi-mode-direction scattering. (c) Extremely asymmetric meta-atom design.

inputs and outputs on each port determines the scattering matrix

$$\begin{bmatrix} \bar{P}_1^{\text{out}} \\ \bar{Q}_2^{\text{out}} \\ \bar{P}_3^{\text{out}} \\ \bar{P}_4^{\text{out}} \\ \bar{P}_5^{\text{out}} \\ \bar{Q}_6^{\text{out}} \\ \bar{P}_7^{\text{out}} \\ \bar{Q}_8^{\text{out}} \end{bmatrix} = \begin{bmatrix} S_{11} & S_{12} & S_{13} & S_{14} & S_{15} & S_{16} & S_{17} & S_{18} \\ S_{21} & S_{22} & S_{23} & S_{24} & S_{25} & S_{26} & S_{27} & S_{28} \\ S_{31} & S_{32} & S_{33} & S_{34} & S_{35} & S_{36} & S_{37} & S_{38} \\ S_{41} & S_{42} & S_{43} & S_{44} & S_{45} & S_{46} & S_{47} & S_{48} \\ S_{51} & S_{52} & S_{53} & S_{54} & S_{55} & S_{56} & S_{57} & S_{58} \\ S_{61} & S_{62} & S_{63} & S_{64} & S_{65} & S_{66} & S_{67} & S_{68} \\ S_{71} & S_{72} & S_{73} & S_{74} & S_{75} & S_{76} & S_{77} & S_{78} \\ S_{81} & S_{82} & S_{83} & S_{84} & S_{85} & S_{86} & S_{87} & S_{88} \end{bmatrix} \begin{bmatrix} \bar{P}_1^{\text{in}} \\ \bar{Q}_2^{\text{in}} \\ \bar{P}_3^{\text{in}} \\ \bar{P}_4^{\text{in}} \\ \bar{P}_5^{\text{in}} \\ \bar{Q}_6^{\text{in}} \\ \bar{P}_7^{\text{in}} \\ \bar{Q}_8^{\text{in}} \end{bmatrix}. \tag{32}$$

The scattering matrix has 8×8 components that can be retrieved through four linearly independent excitations. An interesting phenomenon can be noted that there is no crosstalk among port $1-4$ or $5-8$ owing to Snell's law Eq. (31). The scattering matrix can thus be decomposed into

$$\mathbf{S} = \begin{bmatrix} \mathbf{O} & \hat{\mathbf{S}}^{\text{T}} \\ \hat{\mathbf{S}} & \mathbf{O} \end{bmatrix}. \tag{33}$$

where

$$\hat{\mathbf{S}} = \begin{bmatrix} S_{51} & S_{52} & S_{53} & S_{54} \\ S_{61} & S_{62} & S_{63} & S_{64} \\ S_{71} & S_{72} & S_{73} & S_{74} \\ S_{81} & S_{82} & S_{83} & S_{84} \end{bmatrix}. \tag{34}$$

If only the up and down directions are considered but ignoring left and right, this sub-matrix would appear to be asymmetric as

$$\hat{\mathbf{S}} = \begin{bmatrix} S_{1'1} & S_{1'2} & S_{1'3} & S_{1'4} \\ S_{2'1} & S_{2'2} & S_{2'3} & S_{2'4} \\ S_{3'1} & S_{3'2} & S_{3'3} & S_{3'4} \\ S_{4'1} & S_{4'2} & S_{4'3} & S_{4'4} \end{bmatrix}. \tag{35}$$

m and m' would never coincide as long as the wave is obliquely incident. Therefore, $\hat{\mathbf{S}}$ is allowed to be asymmetric and is termed apparent scattering matrix in this paper. As a note, the designed meta-atom may easily provide an extremely asymmetric response without tangential power flow or the requirement for a horizontally graded design.

The four channels depicted with orange and yellow solid and dashed lines in Fig. 5(b) are given as an example. Assuming it can be implemented, let's check what phenomena we can get under the incidence of transverse or longitudinal waves from the left and right sides, respectively. When a longitudinal wave is incident from the lower left side (excited at port 1), the response in the form of a longitudinal wave can be detected at the upper right side (port 7). But if the incident wave is a longitudinal wave from the lower right side (port 5), we can obtain the refracted transverse wave at the upper left side (port 4). Nevertheless, similar phenomena can be observed if the incident wave is a transverse wave. The transverse wave incident from the lower left (port 2) can be transmitted to the upper right

(port 8) freely. Moreover, the transverse wave incident from the lower right side (port 6) would be converted into a longitudinal wave towards the upper left side (port 3). When the transmittance of all channels reaches 100%, the amplitude of each component of the apparent scattering matrix can be given as

$$\mathrm{abs}\left(\hat{\mathbf{S}}\right) = \begin{bmatrix} 0 & 0 & 0 & 1 \\ 0 & 0 & 1 & 0 \\ 1 & 0 & 0 & 0 \\ 0 & 1 & 0 & 0 \end{bmatrix}, \tag{36}$$

which is obviously asymmetric.

A simple example is given next to illustrate the necessary condition for asymmetric scattering using elastic longitudinal waves without mode coupling. In this case the scattering matrix is simplified as

$$\mathbf{S} = \begin{bmatrix} S_{11} & S_{13} & S_{15} & S_{17} \\ S_{31} & S_{33} & S_{35} & S_{37} \\ S_{51} & S_{53} & S_{55} & S_{57} \\ S_{71} & S_{73} & S_{75} & S_{77} \end{bmatrix}. \tag{37}$$

If the meta-atom is designed to be vertically symmetric and horizontally asymmetric, then

$$S_{17} = S_{35}, \qquad S_{71} = S_{53}. \tag{38}$$

Owing to reciprocity [Eq. (10)], the other off-diagonal components are determined as

$$S_{53} = S_{35} = S_{17} = S_{71}. \tag{39}$$

So, mere left-right asymmetry is not sufficient to support asymmetric scattering. Similarly, if the meta-atom is vertically asymmetric and horizontally symmetric, then

$$S_{17} = S_{53}, \qquad S_{35} = S_{71}. \tag{40}$$

The determination of Eq.(39) again follows. Therefore, the meta-atom needs to be asymmetric both vertically and horizontally.

To achieve completely asymmetric scattering, the structure of the meta-atom in Fig. 1(d) should be modified. The structure of the meta-atom can be arbitrarily given as long as asymmetry is ensured. However, geometric asymmetry is expected to be introduced while preserving the mode conversion capability depicted in Fig. 1(d). Therefore, the structure of Willis metamaterials[100–102] with directivity is introduced to support this asymmetry. The refined structure design for the meta-atom is presented in Fig. 5(c). The connection between the right hand side of the mass block and the rectangular frame is cut. Then it becomes horizontally asymmetric while providing the same compression-torsion coupling as the structure discussed in Sect. III. The structure is naturally vertically asymmetric, so is expected to provide completely asymmetric scattering. The structure in Fig. 5 (c) is optimized to approach the target apparent scattering matrix (see Appendix C for the retrieval procedure o The selected optimization parameters for the extreme asymmetric mode conversion meta-atom are the same as for symmetric meta-atoms as shown in Fig. 1(e), except that the connection between the right side of the mass block and the square frame is removed. The fitness function is set to the minimum value of the transmittance of the target channel

$$f = \min\left(S_{1'3}, S_{2'4}, S_{3'2}, S_{4'1}\right). \tag{41}$$

The left and right boundaries of the background media above and below the meta-atom are set as Bloch-Floquet conditions

$$\mathbf{u}_{\mathrm{left}} = \mathbf{u}_{\mathrm{right}} e^{-ik_P \sin\theta_P w_{\mathrm{cell}}}. \tag{42}$$

Then both longitudinal and transverse wave fields obey Snell's law Eq.(31). Four linearly independent excitations need to be examined to obtain the apparent scattering matrix (see Appendix D for detailed simulation settings). The complete scattering matrix is determined by Eq.(33).

The responses of the optimized meta-atom to excitations at ports $1-8$ are numerically simulated and shown in Figs. 6(a-h) (detailed simulation settings are recorded in Appendix D). Radiation patterns are also provided as a quantitative evaluation with the incident wave as a reference. The incidence of longitudinal waves from the lower left implies excitation at port 1. It can be noted that longitudinal waves are transmitted (to port 7) without conversion to

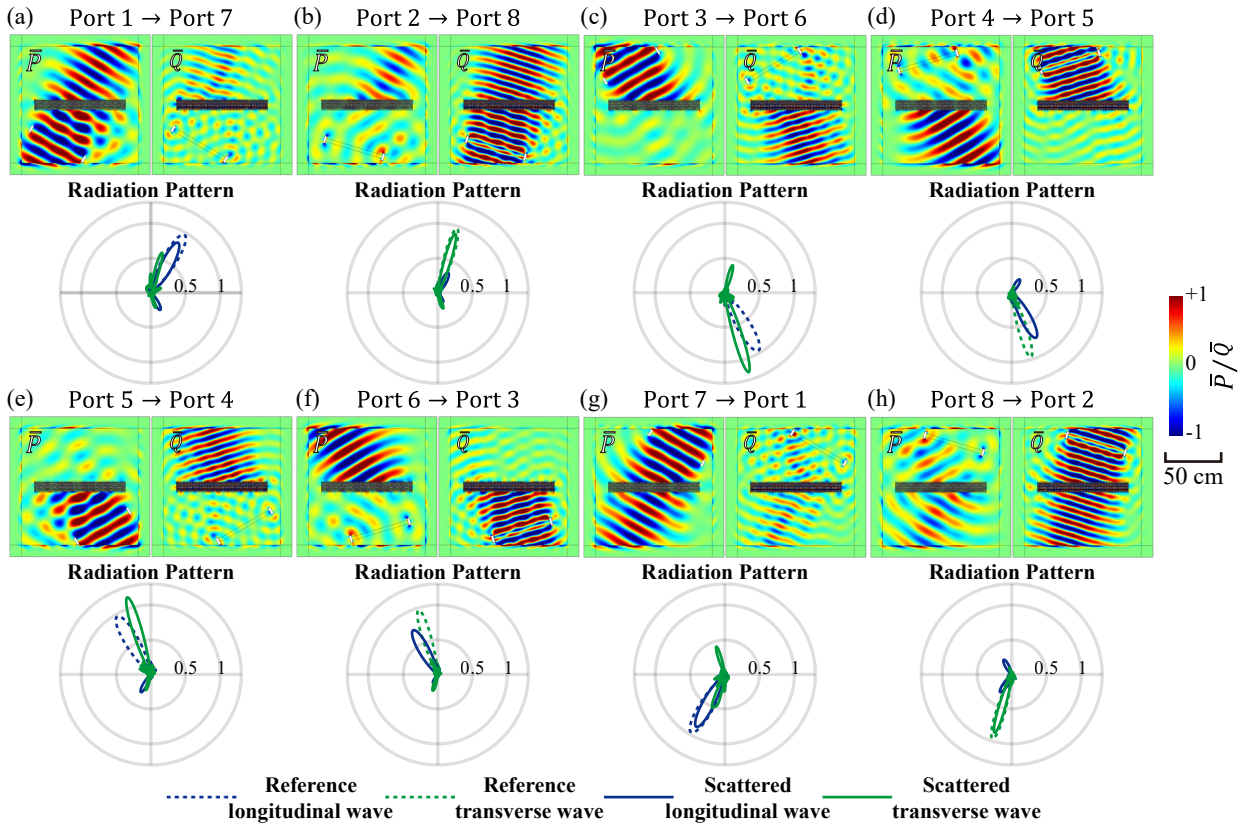

FIG. 6. Collective response of the designed extremely asymmetric meta-atom and corresponding radiation pattern. (a) Response without mode conversion under an incident longitudinal wave from the lower left side. (b) Response without mode conversion under the incident transverse wave from the lower left side. (c) Response with mode conversion under the incident longitudinal wave from the upper left side. (d) Response with mode conversion under the incident transverse wave from the upper left side. (e) Response with mode conversion under the incident longitudinal wave from the lower right side. (f) Response with mode conversion under the incident transverse wave from the lower right side. (g) Response without mode conversion under the incident longitudinal wave from the upper right side. (h) Response without mode conversion under the incident transverse wave from the upper right side.

transverse wave and only some leaked scattering appears in the transverse wave field, as shown in Fig. 6(a). Similarly, transverse waves incident from the lower left (port 2) are also smoothly transmitted (to port 8) with only a little conversion to longitudinal waves, as shown in Fig. 6(b). Contrarily, longitudinal (port 3) and transverse waves (port 4) incident from the upper left are converted into transverse (port 6) and longitudinal waves (port 5), respectively, after passing through the metasurface, as shown in Figs. 6(c) and (d). Because of reciprocity, the responses of metasurfaces are always symmetrical when exchanging excitation and receiving ports. Waves incident from the lower right and the upper left are symmetrical. Incident longitudinal (port 5) and transverse (port 6) waves are converted into transverse (port 4) and longitudinal (port 3) waves towards the upper left, respectively, as shown in Figs. 6(e) and (f). They correspond to the channels depicted with orange and yellow solid lines in Fig. 6(c), respectively. Moreover, the orange and yellow dashed lines in Fig. 4(b) connect ports 1 to 7 and ports 2 to 8, respectively. Therefore, longitudinal (port 7) and transverse (port 8) waves incident on the upper right can be observed to have a symmetrical response compared to those incident on the lower right (ports 1 and 2), as shown in Figs. 6(g) and (h).

V. EXPERIMENTAL VALIDATION

In this section, experiments are conducted on elastic metasurfaces with a scanning laser vibrometer. The samples are fabricated by mechanical machining and measured in time domain to validate the designed meta-atoms.

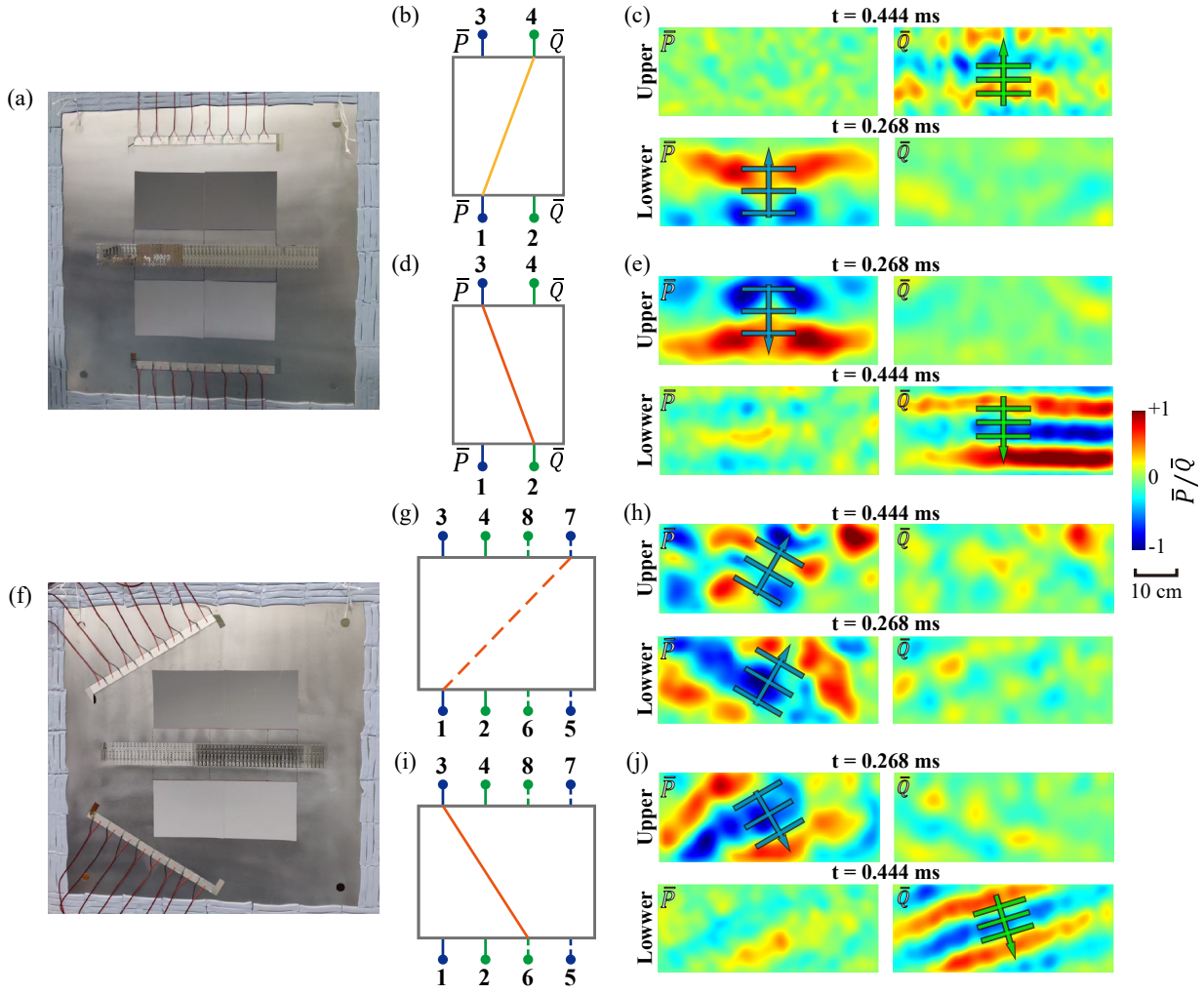

FIG. 7. The experimental sample and results of the designed metasurfaces. (a) Experimental model of transmission symmetric mode conversion metasurface. (b) Schematic diagram of longitudinal-transverse wave mode conversion (from port 1 to port 4). (c) Experimental result of longitudinal-transverse wave mode conversion (from port 1 to port 4). (d) Schematic diagram of longitudinal-transverse wave mode conversion (from port 2 to port 3). (e) Experimental result of longitudinal-transverse wave mode conversion (from port 2 to port 3). (f) Experimental model of asymmetric mode conversion metasurface. (g) Schematic diagram of longitudinal wave transmission without mode conversion (from port 1 to port 7). (h) Experimental result of longitudinal wave transmission without mode conversion (from port 1 to port 7). (i) Schematic diagram of longitudinal transverse wave mode conversion (from port 3 to port 6). (j) Experimental result of longitudinal transverse wave mode conversion (from port 3 to port 6).

Experiments on elastic metasurfaces for transmission symmetric mode conversion, presented in Sect. III, and asymmetric mode conversion, presented in Sect. IV, are conducted to validate the simulation results as shown in Fig. 7 (experimental environment and equipment are detailed in Appendix G). The sample for transmission symmetric mode conversion is shown in Fig. 7(a). The metasurface is located at the center of the board. Two excitation methods are considered, including longitudinal wave incidence from the lower side (excitation at port 1) and longitudinal wave incidence from the upper side (excitation at port 3). The expected response for longitudinal waves incident from the lower side is shown in Fig. 7(b). The upper side of the metasurface should be dominated by transverse waves, while the lower side is dominated by longitudinal waves. The distribution of $\bar{P}$ and $\bar{Q}$ obtained by analyzing the displacement field obtained by laser vibration measurement using Matlab is shown in Fig. 7(c). It can be noted that the incident field is dominated by longitudinal waves and rarely excited by transverse waves. After passing through the metasurface, the transmited field is dominated by transverse waves, and few longitudinal waves can be recognized.

The expected response corresponding to excitation of the incident wave from the upper side is plotted in Fig. 7(d). The upper side of the metasurface should be dominated by longitudinal waves while the lower side is dominated by transverse waves, which is basically consistent with what is shown in Fig. 7(e). It can be noted that the incident longitudinal wave is converted into a transverse wave after passing through the metasurface.

The sample for asymmetric mode conversion is shown in Fig. 7(f). Two excitation methods are considered, including longitudinal wave incidence from the lower left side (excitation at port 1) and longitudinal wave incidence from the upper left side (excitation at port 3). Transmission without mode conversion is expected when longitudinal waves are incident from the lower left side, as shown in Fig. 7(g). It can be noted that both the incident field and the transmitted field are dominated by longitudinal waves, as the experimental results in Fig. 7(h) confirm. The ideal response corresponding to excitation of the incident wave from the lower left side is plotted in Fig. 7(i). The incident longitudinal wave is expected to be converted into a transverse wave, which is consistent with the experimental results shown in Fig. 7(j). It is worth noting that the incident angle is about 30° and the refractive angle is about 16.8°, which follows Snell's law.

VI. CONCLUSIONS

In this paper, a multi-polarization scattering model for the customization of versatile elastic meta-atoms is proposed based on an acoustic-elastic analogy in the frame of the plane stress assumption. Each meta-atom can be characterized as a 4-port model under normal incidence and a 8-port model under oblique incidence. The 4-port model provides two independent channels inside the meta-atom, while the 8-port model provides four independent channels. Each channel inherently supports the integration of a unique function within the meta-atom. A sextuple compression-torsion coupling meta-atom is proposed for the implementation of multi-mode scattering customization. This meta-atom fulfills most requirements for mode manipulation with the help of optimization. Furthermore, after enhancing its geometric asymmetry through the introduction of Willis coupling, it can provide completely asymmetric polarization conversion under oblique incidence. All four internal channels of the 8-port model can be customized, allowing a meta-atom array to selectively provide mode conversion or transmission for specific incident waves.

The meta-atom array considered in this paper is horizontally uniform without tangential gradients. Furthermore, the tangential scale of the meta-atom is deeply sub-wavelength. This indicates that both the 4-port model and the 8-port model are compatible with generalized Snell's law or impedance theory. An elastic metasurface could then provide two or four different functions for multi-mode wavefront manipulation. Moreover, the 8-port model has potential worth exploring, since there are at least 24 possible connection methods for channels within the meta-atom. This model can also be extended to mode manipulation of 3D elastic fields, which would result in more channels being established in a single meta-atom. The versatility of metasurfaces could then be further enhanced. However, the thickness of the metasurface might become a disadvantage as the six compression-torsion coupling substructures need to be connected in series. It is not yet clear which minimum number of substructures is required to implement an arbitrary scattering matrix. Subsequent work will be devoted to integrating richer functions in a single elastic metasurface and miniaturizing its structural dimensions.

VII. DATA AVAILABILITY

The data that support the findings of this study are available from the corresponding authors upon reasonable request.

VIII. ACKNOWLEDGMENTS

The authors acknowledge financial support by the National Natural Science Foundation of China (124B2034 and 12021002). V.L. acknowledges financial support by the EIPHI Graduate School (ANR-17-EURE-0002).

IX. COMPETING INTERESTS

The authors declare no competing interests.

X. AUTHOR CONTRIBUTIONS

Y.Z.T. developed the mathematical model, performed simulations and wrote the paper, Y.M.C. fabricated the samples and realized the experiments; L.Y.C. guided the research; Y.F.W. and V.L. guided the research and reviewed the manuscript; Y.S.W. supervised the project. All authors contributed to data analysis and discussions.

Appendix A: Determination of components in elastic impedance matrix

The components on the left side of Eq. (20) are directly given as

$$P|_{y_1=0} = \alpha_1 m_1 + \alpha_2 m_2 + \alpha_3 m_1 + \alpha_4 m_2 = A_1\alpha_1 + B_1\alpha_2 + C_1\alpha_3 + D_1\alpha_4, \tag{A1}$$

$$Q|_{y_1=0} = \alpha_1 n_1 + \alpha_2 n_2 + \alpha_3 n_1 + \alpha_4 n_2 = A_2\alpha_1 + B_2\alpha_2 + C_2\alpha_3 + D_2\alpha_4, \tag{A2}$$

$$P|_{y_1=h_0} = \alpha_1 m_1 e^{\imath\sqrt{r_1}h_0} + \alpha_2 m_2 e^{\imath\sqrt{r_2}h_0} + \alpha_3 m_1 e^{-\imath\sqrt{r_1}h_0} + \alpha_4 m_2 e^{-\imath\sqrt{r_2}h_0} = A_3\alpha_1 + B_3\alpha_2 + C_3\alpha_3 + D_3\alpha_4, \tag{A3}$$

$$Q|_{y_1=h_0} = \alpha_1 n_1 e^{\imath\sqrt{r_1}h_0} + \alpha_2 n_2 e^{\imath\sqrt{r_2}h_0} + \alpha_3 n_1 e^{-\imath\sqrt{r_1}h_0} + \alpha_4 n_2 e^{-\imath\sqrt{r_2}h_0} = A_4\alpha_1 + B_4\alpha_2 + C_4\alpha_3 + D_4\alpha_4. \tag{A4}$$

Substituting Eq. (19) into Eq. (14), part of the components can be calculated as

$$\left.\frac{\partial P}{\partial y}\right|_{y_1=0} = \imath\alpha_1\sqrt{r_1}m_1 + \imath\alpha_2\sqrt{r_2}m_2 - \imath\alpha_3\sqrt{r_1}m_1 - \imath\alpha_4\sqrt{r_2}m_2 = A_5\alpha_1 + B_5\alpha_2 + C_5\alpha_3 + D_5\alpha_4, \tag{A5}$$

$$\left.\frac{\partial Q}{\partial y}\right|_{y_1=0} = \imath\alpha_1\sqrt{r_1}n_1 + \imath\alpha_2\sqrt{r_2}n_2 - \imath\alpha_3\sqrt{r_1}n_1 - \imath\alpha_4\sqrt{r_2}n_2 = A_6\alpha_1 + B_6\alpha_2 + C_6\alpha_3 + D_6\alpha_4, \tag{A6}$$

$$\left.\frac{\partial P}{\partial y}\right|_{y_1=h_0} = \imath\alpha_1\sqrt{r_1}m_1 e^{\imath\sqrt{r_1}h_0} + \imath\alpha_2\sqrt{r_2}m_2 e^{\imath\sqrt{r_1}h_0} - \imath\alpha_3\sqrt{r_1}m_1 e^{\imath\sqrt{r_1}h_0} - \imath\alpha_4\sqrt{r_2}m_2 e^{\imath\sqrt{r_1}h_0} = A_7\alpha_1 + B_7\alpha_2 + C_7\alpha_3 + D_7\alpha_4, \tag{A7}$$

$$\left.\frac{\partial Q}{\partial y}\right|_{y_1=h_0} = \imath\alpha_1\sqrt{r_1}n_1 e^{\imath\sqrt{r_1}h_0} + \imath\alpha_2\sqrt{r_2}n_2 e^{\imath\sqrt{r_1}h_0} - \imath\alpha_3\sqrt{r_1}n_1 e^{\imath\sqrt{r_1}h_0} - \imath\alpha_4\sqrt{r_2}n_2 e^{\imath\sqrt{r_1}h_0} = A_8\alpha_1 + B_8\alpha_2 + C_8\alpha_3 + D_8\alpha_4. \tag{A8}$$

Substituting Eqs. (A5-A8) back into the right part of Eq. (20), they become

$$\begin{bmatrix} -\mathbf{n}_1\cdot\mathbf{v}_P|_1 \\ -\mathbf{n}_1\cdot\mathbf{v}_Q|_1 \\ -\mathbf{n}_2\cdot\mathbf{v}_P|_2 \\ -\mathbf{n}_2\cdot\mathbf{v}_Q|_2 \end{bmatrix} = \begin{bmatrix} \frac{\imath}{\omega_0}\left[\frac{1}{\rho_P}\left(A_5\alpha_1 + B_5\alpha_2 + C_5\alpha_3 + D_5\alpha_4\right) + \frac{b}{\rho_0}\left(A_6\alpha_1 + B_6\alpha_2 + C_6\alpha_3 + D_6\alpha_4\right)\right] \\ \frac{\imath}{\omega_0}\left[\frac{b}{\rho_0}\left(A_5\alpha_1 + B_5\alpha_2 + C_5\alpha_3 + D_5\alpha_4\right) + \frac{1}{\rho_Q}\left(A_6\alpha_1 + B_6\alpha_2 + C_6\alpha_3 + D_6\alpha_4\right)\right] \\ -\frac{\imath}{\omega_0}\left[\frac{1}{\rho_P}\left(A_7\alpha_1 + B_7\alpha_2 + C_7\alpha_3 + D_7\alpha_4\right) + \frac{b}{\rho_0}\left(A_8\alpha_1 + B_8\alpha_2 + C_8\alpha_3 + D_8\alpha_4\right)\right] \\ -\frac{\imath}{\omega_0}\left[\frac{b}{\rho_0}\left(A_7\alpha_1 + B_7\alpha_2 + C_7\alpha_3 + D_7\alpha_4\right) + \frac{1}{\rho_Q}\left(A_8\alpha_1 + B_8\alpha_2 + C_8\alpha_3 + D_8\alpha_4\right)\right] \end{bmatrix} \tag{A9}$$

Then, the first to fourth lines of Eq. (20) can be reorganized as

$$\begin{aligned} &\left[-A_1 + Z_{11}\frac{\imath}{\omega_0}\left(\frac{A_5}{\rho_P} + \frac{bA_6}{\rho_0}\right) + Z_{12}\frac{\imath}{\omega_0}\left(\frac{bA_5}{\rho_0} + \frac{A_6}{\rho_Q}\right) - Z_{13}\frac{\imath}{\omega_0}\left(\frac{A_7}{\rho_P} + \frac{bA_8}{\rho_0}\right) - Z_{14}\frac{\imath}{\omega_0}\left(\frac{bA_7}{\rho_0} + \frac{A_8}{\rho_Q}\right)\right]\alpha_1 + \\ &\left[-B_1 + Z_{11}\frac{\imath}{\omega_0}\left(\frac{B_5}{\rho_P} + \frac{bB_6}{\rho_0}\right) + Z_{12}\frac{\imath}{\omega_0}\left(\frac{bB_5}{\rho_0} + \frac{B_6}{\rho_Q}\right) - Z_{13}\frac{\imath}{\omega_0}\left(\frac{B_7}{\rho_P} + \frac{bB_8}{\rho_0}\right) - Z_{14}\frac{\imath}{\omega_0}\left(\frac{bB_7}{\rho_0} + \frac{B_8}{\rho_Q}\right)\right]\alpha_2 + \\ &\left[-C_1 + Z_{11}\frac{\imath}{\omega_0}\left(\frac{C_5}{\rho_P} + \frac{bC_6}{\rho_0}\right) + Z_{12}\frac{\imath}{\omega_0}\left(\frac{bC_5}{\rho_0} + \frac{C_6}{\rho_Q}\right) - Z_{13}\frac{\imath}{\omega_0}\left(\frac{C_7}{\rho_P} + \frac{bC_8}{\rho_0}\right) - Z_{14}\frac{\imath}{\omega_0}\left(\frac{bC_7}{\rho_0} + \frac{C_8}{\rho_Q}\right)\right]\alpha_3 + \\ &\left[-D_1 + Z_{11}\frac{\imath}{\omega_0}\left(\frac{D_5}{\rho_P} + \frac{bD_6}{\rho_0}\right) + Z_{12}\frac{\imath}{\omega_0}\left(\frac{bD_5}{\rho_0} + \frac{D_6}{\rho_Q}\right) - Z_{13}\frac{\imath}{\omega_0}\left(\frac{D_7}{\rho_P} + \frac{bD_8}{\rho_0}\right) - Z_{14}\frac{\imath}{\omega_0}\left(\frac{bD_7}{\rho_0} + \frac{D_8}{\rho_Q}\right)\right]\alpha_4 = 0 \end{aligned} \tag{A10}$$

$$\left[-A_2+Z_{21}\frac{\imath}{\omega_0}\left(\frac{A_5}{\rho_P}+\frac{bA_6}{\rho_0}\right)+Z_{22}\frac{\imath}{\omega_0}\left(\frac{bA_5}{\rho_0}+\frac{A_6}{\rho_Q}\right)-Z_{23}\frac{\imath}{\omega_0}\left(\frac{A_7}{\rho_P}+\frac{bA_8}{\rho_0}\right)-Z_{24}\frac{\imath}{\omega_0}\left(\frac{bA_7}{\rho_0}+\frac{A_8}{\rho_Q}\right)\right]\alpha_1+$$
$$\left[-B_2+Z_{21}\frac{\imath}{\omega_0}\left(\frac{B_5}{\rho_P}+\frac{bB_6}{\rho_0}\right)+Z_{22}\frac{\imath}{\omega_0}\left(\frac{bB_5}{\rho_0}+\frac{B_6}{\rho_Q}\right)-Z_{23}\frac{\imath}{\omega_0}\left(\frac{B_7}{\rho_P}+\frac{bB_8}{\rho_0}\right)-Z_{24}\frac{\imath}{\omega_0}\left(\frac{bB_7}{\rho_0}+\frac{B_8}{\rho_Q}\right)\right]\alpha_2+$$
$$\left[-C_2+Z_{21}\frac{\imath}{\omega_0}\left(\frac{C_5}{\rho_P}+\frac{bC_6}{\rho_0}\right)+Z_{22}\frac{\imath}{\omega_0}\left(\frac{bC_5}{\rho_0}+\frac{C_6}{\rho_Q}\right)-Z_{23}\frac{\imath}{\omega_0}\left(\frac{C_7}{\rho_P}+\frac{bC_8}{\rho_0}\right)-Z_{24}\frac{\imath}{\omega_0}\left(\frac{bC_7}{\rho_0}+\frac{C_8}{\rho_Q}\right)\right]\alpha_3+$$
$$\left[-D_2+Z_{21}\frac{\imath}{\omega_0}\left(\frac{D_5}{\rho_P}+\frac{bD_6}{\rho_0}\right)+Z_{22}\frac{\imath}{\omega_0}\left(\frac{bD_5}{\rho_0}+\frac{D_6}{\rho_Q}\right)-Z_{23}\frac{\imath}{\omega_0}\left(\frac{D_7}{\rho_P}+\frac{bD_8}{\rho_0}\right)-Z_{24}\frac{\imath}{\omega_0}\left(\frac{bD_7}{\rho_0}+\frac{D_8}{\rho_Q}\right)\right]\alpha_4=0 \tag{A11}$$

$$\left[-A_3+Z_{31}\frac{\imath}{\omega_0}\left(\frac{A_5}{\rho_P}+\frac{bA_6}{\rho_0}\right)+Z_{32}\frac{\imath}{\omega_0}\left(\frac{bA_5}{\rho_0}+\frac{A_6}{\rho_Q}\right)-Z_{33}\frac{\imath}{\omega_0}\left(\frac{A_7}{\rho_P}+\frac{bA_8}{\rho_0}\right)-Z_{34}\frac{\imath}{\omega_0}\left(\frac{bA_7}{\rho_0}+\frac{A_8}{\rho_Q}\right)\right]\alpha_1+$$
$$\left[-B_3+Z_{31}\frac{\imath}{\omega_0}\left(\frac{B_5}{\rho_P}+\frac{bB_6}{\rho_0}\right)+Z_{32}\frac{\imath}{\omega_0}\left(\frac{bB_5}{\rho_0}+\frac{B_6}{\rho_Q}\right)-Z_{33}\frac{\imath}{\omega_0}\left(\frac{B_7}{\rho_P}+\frac{bB_8}{\rho_0}\right)-Z_{34}\frac{\imath}{\omega_0}\left(\frac{bB_7}{\rho_0}+\frac{B_8}{\rho_Q}\right)\right]\alpha_2+$$
$$\left[-C_3+Z_{31}\frac{\imath}{\omega_0}\left(\frac{C_5}{\rho_P}+\frac{bC_6}{\rho_0}\right)+Z_{32}\frac{\imath}{\omega_0}\left(\frac{bC_5}{\rho_0}+\frac{C_6}{\rho_Q}\right)-Z_{33}\frac{\imath}{\omega_0}\left(\frac{C_7}{\rho_P}+\frac{bC_8}{\rho_0}\right)-Z_{34}\frac{\imath}{\omega_0}\left(\frac{bC_7}{\rho_0}+\frac{C_8}{\rho_Q}\right)\right]\alpha_3+$$
$$\left[-D_3+Z_{31}\frac{\imath}{\omega_0}\left(\frac{D_5}{\rho_P}+\frac{bD_6}{\rho_0}\right)+Z_{32}\frac{\imath}{\omega_0}\left(\frac{bD_5}{\rho_0}+\frac{D_6}{\rho_Q}\right)-Z_{33}\frac{\imath}{\omega_0}\left(\frac{D_7}{\rho_P}+\frac{bD_8}{\rho_0}\right)-Z_{34}\frac{\imath}{\omega_0}\left(\frac{bD_7}{\rho_0}+\frac{D_8}{\rho_Q}\right)\right]\alpha_4=0 \tag{A12}$$

$$\left[-A_4+Z_{41}\frac{\imath}{\omega_0}\left(\frac{A_5}{\rho_P}+\frac{bA_6}{\rho_0}\right)+Z_{42}\frac{\imath}{\omega_0}\left(\frac{bA_5}{\rho_0}+\frac{A_6}{\rho_Q}\right)-Z_{43}\frac{\imath}{\omega_0}\left(\frac{A_7}{\rho_P}+\frac{bA_8}{\rho_0}\right)-Z_{44}\frac{\imath}{\omega_0}\left(\frac{bA_7}{\rho_0}+\frac{A_8}{\rho_Q}\right)\right]\alpha_1+$$
$$\left[-B_4+Z_{41}\frac{\imath}{\omega_0}\left(\frac{B_5}{\rho_P}+\frac{bB_6}{\rho_0}\right)+Z_{42}\frac{\imath}{\omega_0}\left(\frac{bB_5}{\rho_0}+\frac{B_6}{\rho_Q}\right)-Z_{43}\frac{\imath}{\omega_0}\left(\frac{B_7}{\rho_P}+\frac{bB_8}{\rho_0}\right)-Z_{44}\frac{\imath}{\omega_0}\left(\frac{bB_7}{\rho_0}+\frac{B_8}{\rho_Q}\right)\right]\alpha_2+$$
$$\left[-C_4+Z_{41}\frac{\imath}{\omega_0}\left(\frac{C_5}{\rho_P}+\frac{bC_6}{\rho_0}\right)+Z_{42}\frac{\imath}{\omega_0}\left(\frac{bC_5}{\rho_0}+\frac{C_6}{\rho_Q}\right)-Z_{43}\frac{\imath}{\omega_0}\left(\frac{C_7}{\rho_P}+\frac{bC_8}{\rho_0}\right)-Z_{44}\frac{\imath}{\omega_0}\left(\frac{bC_7}{\rho_0}+\frac{C_8}{\rho_Q}\right)\right]\alpha_3+$$
$$\left[-D_4+Z_{41}\frac{\imath}{\omega_0}\left(\frac{D_5}{\rho_P}+\frac{bD_6}{\rho_0}\right)+Z_{42}\frac{\imath}{\omega_0}\left(\frac{bD_5}{\rho_0}+\frac{D_6}{\rho_Q}\right)-Z_{43}\frac{\imath}{\omega_0}\left(\frac{D_7}{\rho_P}+\frac{bD_8}{\rho_0}\right)-Z_{44}\frac{\imath}{\omega_0}\left(\frac{bD_7}{\rho_0}+\frac{D_8}{\rho_Q}\right)\right]\alpha_4=0 \tag{A13}$$

Because the impedance matrix $\mathbf{S}$ is an inherent property of the material, it should be independent of $\alpha_i\,(i=1-4)$. The coefficient of $\alpha_i\,(i=1-4)$ should always be zero, so the components of the impedance matrix should obey

$$\begin{bmatrix}\frac{\imath}{\omega_0}\left(\frac{A_5}{\rho_P}+\frac{bA_6}{\rho_0}\right) & \frac{\imath}{\omega_0}\left(\frac{bA_5}{\rho_0}+\frac{A_6}{\rho_Q}\right) & -\frac{\imath}{\omega_0}\left(\frac{A_7}{\rho_P}+\frac{bA_8}{\rho_0}\right) & -\frac{\imath}{\omega_0}\left(\frac{bA_7}{\rho_0}+\frac{A_8}{\rho_Q}\right)\\ \frac{\imath}{\omega_0}\left(\frac{B_5}{\rho_P}+\frac{bB_6}{\rho_0}\right) & \frac{\imath}{\omega_0}\left(\frac{bB_5}{\rho_0}+\frac{B_6}{\rho_Q}\right) & -\frac{\imath}{\omega_0}\left(\frac{B_7}{\rho_P}+\frac{bB_8}{\rho_0}\right) & -\frac{\imath}{\omega_0}\left(\frac{bB_7}{\rho_0}+\frac{B_8}{\rho_Q}\right)\\ \frac{\imath}{\omega_0}\left(\frac{C_5}{\rho_P}+\frac{bC_6}{\rho_0}\right) & \frac{\imath}{\omega_0}\left(\frac{bC_5}{\rho_0}+\frac{C_6}{\rho_Q}\right) & -\frac{\imath}{\omega_0}\left(\frac{C_7}{\rho_P}+\frac{bC_8}{\rho_0}\right) & -\frac{\imath}{\omega_0}\left(\frac{bC_7}{\rho_0}+\frac{C_8}{\rho_Q}\right)\\ \frac{\imath}{\omega_0}\left(\frac{D_5}{\rho_P}+\frac{bD_6}{\rho_0}\right) & \frac{\imath}{\omega_0}\left(\frac{bD_5}{\rho_0}+\frac{D_6}{\rho_Q}\right) & -\frac{\imath}{\omega_0}\left(\frac{D_7}{\rho_P}+\frac{bD_8}{\rho_0}\right) & -\frac{\imath}{\omega_0}\left(\frac{bD_7}{\rho_0}+\frac{D_8}{\rho_Q}\right)\end{bmatrix}\begin{bmatrix}Z_{11}\\Z_{12}\\Z_{13}\\Z_{14}\end{bmatrix}=\begin{bmatrix}A_1\\B_1\\C_1\\D_1\end{bmatrix}, \tag{A14}$$

$$\begin{bmatrix}\frac{\imath}{\omega_0}\left(\frac{A_5}{\rho_P}+\frac{bA_6}{\rho_0}\right) & \frac{\imath}{\omega_0}\left(\frac{bA_5}{\rho_0}+\frac{A_6}{\rho_Q}\right) & -\frac{\imath}{\omega_0}\left(\frac{A_7}{\rho_P}+\frac{bA_8}{\rho_0}\right) & -\frac{\imath}{\omega_0}\left(\frac{bA_7}{\rho_0}+\frac{A_8}{\rho_Q}\right)\\ \frac{\imath}{\omega_0}\left(\frac{B_5}{\rho_P}+\frac{bB_6}{\rho_0}\right) & \frac{\imath}{\omega_0}\left(\frac{bB_5}{\rho_0}+\frac{B_6}{\rho_Q}\right) & -\frac{\imath}{\omega_0}\left(\frac{B_7}{\rho_P}+\frac{bB_8}{\rho_0}\right) & -\frac{\imath}{\omega_0}\left(\frac{bB_7}{\rho_0}+\frac{B_8}{\rho_Q}\right)\\ \frac{\imath}{\omega_0}\left(\frac{C_5}{\rho_P}+\frac{bC_6}{\rho_0}\right) & \frac{\imath}{\omega_0}\left(\frac{bC_5}{\rho_0}+\frac{C_6}{\rho_Q}\right) & -\frac{\imath}{\omega_0}\left(\frac{C_7}{\rho_P}+\frac{bC_8}{\rho_0}\right) & -\frac{\imath}{\omega_0}\left(\frac{bC_7}{\rho_0}+\frac{C_8}{\rho_Q}\right)\\ \frac{\imath}{\omega_0}\left(\frac{D_5}{\rho_P}+\frac{bD_6}{\rho_0}\right) & \frac{\imath}{\omega_0}\left(\frac{bD_5}{\rho_0}+\frac{D_6}{\rho_Q}\right) & -\frac{\imath}{\omega_0}\left(\frac{D_7}{\rho_P}+\frac{bD_8}{\rho_0}\right) & -\frac{\imath}{\omega_0}\left(\frac{bD_7}{\rho_0}+\frac{D_8}{\rho_Q}\right)\end{bmatrix}\begin{bmatrix}Z_{21}\\Z_{22}\\Z_{23}\\Z_{24}\end{bmatrix}=\begin{bmatrix}A_2\\B_2\\C_2\\D_2\end{bmatrix}, \tag{A15}$$

$$\begin{bmatrix}\frac{\imath}{\omega_0}\left(\frac{A_5}{\rho_P}+\frac{bA_6}{\rho_0}\right) & \frac{\imath}{\omega_0}\left(\frac{bA_5}{\rho_0}+\frac{A_6}{\rho_Q}\right) & -\frac{\imath}{\omega_0}\left(\frac{A_7}{\rho_P}+\frac{bA_8}{\rho_0}\right) & -\frac{\imath}{\omega_0}\left(\frac{bA_7}{\rho_0}+\frac{A_8}{\rho_Q}\right)\\ \frac{\imath}{\omega_0}\left(\frac{B_5}{\rho_P}+\frac{bB_6}{\rho_0}\right) & \frac{\imath}{\omega_0}\left(\frac{bB_5}{\rho_0}+\frac{B_6}{\rho_Q}\right) & -\frac{\imath}{\omega_0}\left(\frac{B_7}{\rho_P}+\frac{bB_8}{\rho_0}\right) & -\frac{\imath}{\omega_0}\left(\frac{bB_7}{\rho_0}+\frac{B_8}{\rho_Q}\right)\\ \frac{\imath}{\omega_0}\left(\frac{C_5}{\rho_P}+\frac{bC_6}{\rho_0}\right) & \frac{\imath}{\omega_0}\left(\frac{bC_5}{\rho_0}+\frac{C_6}{\rho_Q}\right) & -\frac{\imath}{\omega_0}\left(\frac{C_7}{\rho_P}+\frac{bC_8}{\rho_0}\right) & -\frac{\imath}{\omega_0}\left(\frac{bC_7}{\rho_0}+\frac{C_8}{\rho_Q}\right)\\ \frac{\imath}{\omega_0}\left(\frac{D_5}{\rho_P}+\frac{bD_6}{\rho_0}\right) & \frac{\imath}{\omega_0}\left(\frac{bD_5}{\rho_0}+\frac{D_6}{\rho_Q}\right) & -\frac{\imath}{\omega_0}\left(\frac{D_7}{\rho_P}+\frac{bD_8}{\rho_0}\right) & -\frac{\imath}{\omega_0}\left(\frac{bD_7}{\rho_0}+\frac{D_8}{\rho_Q}\right)\end{bmatrix}\begin{bmatrix}Z_{31}\\Z_{32}\\Z_{33}\\Z_{34}\end{bmatrix}=\begin{bmatrix}A_3\\B_3\\C_3\\D_3\end{bmatrix}, \tag{A16}$$

$$\begin{bmatrix} \frac{\imath}{\omega_0}\left(\frac{A_5}{\rho_P}+\frac{bA_6}{\rho_0}\right) & \frac{\imath}{\omega_0}\left(\frac{bA_5}{\rho_0}+\frac{A_6}{\rho_Q}\right) & -\frac{\imath}{\omega_0}\left(\frac{A_7}{\rho_P}+\frac{bA_8}{\rho_0}\right) & -\frac{\imath}{\omega_0}\left(\frac{bA_7}{\rho_0}+\frac{A_8}{\rho_Q}\right) \\ \frac{\imath}{\omega_0}\left(\frac{B_5}{\rho_P}+\frac{bB_6}{\rho_0}\right) & \frac{\imath}{\omega_0}\left(\frac{bB_5}{\rho_0}+\frac{B_6}{\rho_Q}\right) & -\frac{\imath}{\omega_0}\left(\frac{B_7}{\rho_P}+\frac{bB_8}{\rho_0}\right) & -\frac{\imath}{\omega_0}\left(\frac{bB_7}{\rho_0}+\frac{B_8}{\rho_Q}\right) \\ \frac{\imath}{\omega_0}\left(\frac{C_5}{\rho_P}+\frac{bC_6}{\rho_0}\right) & \frac{\imath}{\omega_0}\left(\frac{bC_5}{\rho_0}+\frac{C_6}{\rho_Q}\right) & -\frac{\imath}{\omega_0}\left(\frac{C_7}{\rho_P}+\frac{bC_8}{\rho_0}\right) & -\frac{\imath}{\omega_0}\left(\frac{bC_7}{\rho_0}+\frac{C_8}{\rho_Q}\right) \\ \frac{\imath}{\omega_0}\left(\frac{D_5}{\rho_P}+\frac{bD_6}{\rho_0}\right) & \frac{\imath}{\omega_0}\left(\frac{bD_5}{\rho_0}+\frac{D_6}{\rho_Q}\right) & -\frac{\imath}{\omega_0}\left(\frac{D_7}{\rho_P}+\frac{bD_8}{\rho_0}\right) & -\frac{\imath}{\omega_0}\left(\frac{bD_7}{\rho_0}+\frac{D_8}{\rho_Q}\right) \end{bmatrix} \begin{bmatrix} Z_{41} \\ Z_{42} \\ Z_{43} \\ Z_{44} \end{bmatrix} = \begin{bmatrix} A_4 \\ B_4 \\ C_4 \\ D_4 \end{bmatrix}, \tag{A17}$$

Then all components of the impedance matrix can be acquired.

Appendix B: Determination of the specific solution through Newton's iteration

Through the method given in Appendix A, one can obtain the impedance matrix $\mathbf{Z}$ corresponding to any set of parameters $\mathbf{q} = \{a, b, c, d, e\}$. After normalization with Eq. (21), the scattering matrix can be obtained by substitution into Eq. (22). The entire process can be represented as a function $\mathbf{S}(\mathbf{q})$. Then, for the objective scattering matrix $\mathbf{S}^{\mathrm{obj}}$, the equation that needs to be solved can be determined as

$$f(\mathbf{q}) = \left\| \left|\mathbf{S}^{\mathrm{obj}}\right| - \left|\mathbf{S}(\mathbf{q})\right| \right\| = 0. \tag{B1}$$

The Jacobian matrix is defined as

$$\mathbf{J}(\mathbf{q}) = \frac{\partial f}{\partial \mathbf{q}}. \tag{B2}$$

Newton iteration can be implemented through

$$\mathbf{q}_{i+1} = \mathbf{q}_i - f(\mathbf{q}_i)\left[\left(\mathbf{J}(\mathbf{q}_i)^T \mathbf{J}(\mathbf{q}_i)\right)^{-1} \mathbf{J}(\mathbf{q}_i)\right]. \tag{B3}$$

Appendix C: Retrieval of scattering matrix

1. Scattering matrix for 4-port model

For each excitation, the response obey the impedance relationship on both boundary of the meta-atom

$$\begin{bmatrix} P|_1 \\ Q|_1 \\ P|_2 \\ Q|_2 \end{bmatrix} = \begin{bmatrix} Z_{11} & Z_{12} & Z_{13} & Z_{14} \\ Z_{21} & Z_{22} & Z_{23} & Z_{24} \\ Z_{31} & Z_{32} & Z_{33} & Z_{34} \\ Z_{41} & Z_{42} & Z_{43} & Z_{44} \end{bmatrix} \begin{bmatrix} -\mathbf{n}_1 \cdot \mathbf{v}_P|_1 \\ -\mathbf{n}_1 \cdot \mathbf{v}_Q|_1 \\ -\mathbf{n}_2 \cdot \mathbf{v}_P|_2 \\ -\mathbf{n}_2 \cdot \mathbf{v}_Q|_2 \end{bmatrix} = -\mathbf{Z} \begin{bmatrix} \mathbf{n}_1 \cdot \mathbf{v}_P|_1 \\ \mathbf{n}_1 \cdot \mathbf{v}_Q|_1 \\ \mathbf{n}_2 \cdot \mathbf{v}_P|_2 \\ \mathbf{n}_2 \cdot \mathbf{v}_Q|_2 \end{bmatrix}. \tag{C1}$$

By exciting the meta-atom twice, one can obtain

$$\begin{bmatrix} P_1|_1 & P_2|_1 \\ Q_1|_1 & Q_2|_1 \\ P_1|_2 & P_2|_2 \\ Q_1|_2 & Q_2|_2 \end{bmatrix} = -\mathbf{Z} \begin{bmatrix} \mathbf{n}_1 \cdot \mathbf{v}_{P_1}|_1 & \mathbf{n}_1 \cdot \mathbf{v}_{P_2}|_1 \\ \mathbf{n}_1 \cdot \mathbf{v}_{Q_1}|_1 & \mathbf{n}_1 \cdot \mathbf{v}_{Q_2}|_1 \\ \mathbf{n}_2 \cdot \mathbf{v}_{P_1}|_2 & \mathbf{n}_2 \cdot \mathbf{v}_{P_2}|_2 \\ \mathbf{n}_2 \cdot \mathbf{v}_{Q_1}|_2 & \mathbf{n}_2 \cdot \mathbf{v}_{Q_2}|_2 \end{bmatrix}, \tag{C2}$$

where the number in the lower corner indicates the number of times it is excited. Since the impedance matrix is purely imaginary for this passive system

$$\mathbf{Z} = \imath \begin{bmatrix} X_{11} & X_{12} & X_{13} & X_{14} \\ X_{21} & X_{22} & X_{23} & X_{24} \\ X_{31} & X_{32} & X_{33} & X_{34} \\ X_{41} & X_{42} & X_{43} & X_{44} \end{bmatrix} = \imath \mathbf{X} \tag{C3}$$

a system of real number equations can be established by separating the real part and the imaginary part of Eq. (C2)

$$\begin{bmatrix} \mathrm{Re}[P_1|_1] & \mathrm{Im}[P_2|_1] & \mathrm{Re}[P_1|_1] & \mathrm{Im}[P_2|_1] \\ \mathrm{Re}[Q_1|_1] & \mathrm{Im}[Q_2|_1] & \mathrm{Re}[Q_1|_1] & \mathrm{Im}[Q_2|_1] \\ \mathrm{Re}[P_1|_2] & \mathrm{Im}[P_2|_2] & \mathrm{Re}[P_1|_2] & \mathrm{Im}[P_2|_2] \\ \mathrm{Re}[Q_1|_2] & \mathrm{Im}[Q_2|_2] & \mathrm{Re}[Q_1|_2] & \mathrm{Im}[Q_2|_2] \end{bmatrix} = -X \begin{bmatrix} \mathrm{Re}[\imath\mathbf{n}_1 \cdot \mathbf{v}_{P_1}|_1] & \mathrm{Re}[\imath\mathbf{n}_1 \cdot \mathbf{v}_{P_2}|_1] & \mathrm{Im}[\imath\mathbf{n}_1 \cdot \mathbf{v}_{P_1}|_1] & \mathrm{Im}[\imath\mathbf{n}_1 \cdot \mathbf{v}_{P_2}|_1] \\ \mathrm{Re}[\imath\mathbf{n}_1 \cdot \mathbf{v}_{Q_1}|_1] & \mathrm{Re}[\imath\mathbf{n}_1 \cdot \mathbf{v}_{Q_2}|_1] & \mathrm{Im}[\imath\mathbf{n}_1 \cdot \mathbf{v}_{Q_1}|_1] & \mathrm{Im}[\imath\mathbf{n}_1 \cdot \mathbf{v}_{Q_2}|_1] \\ \mathrm{Re}[\imath\mathbf{n}_2 \cdot \mathbf{v}_{P_1}|_2] & \mathrm{Re}[\imath\mathbf{n}_2 \cdot \mathbf{v}_{P_2}|_2] & \mathrm{Im}[\imath\mathbf{n}_2 \cdot \mathbf{v}_{P_1}|_2] & \mathrm{Im}[\imath\mathbf{n}_2 \cdot \mathbf{v}_{P_2}|_2] \\ \mathrm{Re}[\imath\mathbf{n}_2 \cdot \mathbf{v}_{Q_1}|_2] & \mathrm{Re}[\imath\mathbf{n}_2 \cdot \mathbf{v}_{Q_2}|_2] & \mathrm{Im}[\imath\mathbf{n}_2 \cdot \mathbf{v}_{Q_1}|_2] & \mathrm{Im}[\imath\mathbf{n}_2 \cdot \mathbf{v}_{Q_2}|_2] \end{bmatrix}. \tag{C4}$$

The impedance matrix can be solved directly. It should be noted that the two excitations must be linearly independent, otherwise Eq. (C4) would have infinitely solutions. The scattering matrix can then be calculated through Eqs. (20) and (21).

2. Scattering matrix for 8-port model

The input and response of the meta-atom under oblique incidence always obey

$$\begin{bmatrix} \bar{P}_1^{\text{out}} \\ \bar{Q}_2^{\text{out}} \\ \bar{P}_3^{\text{out}} \\ \bar{P}_4^{\text{out}} \\ \bar{P}_5^{\text{out}} \\ \bar{Q}_6^{\text{out}} \\ \bar{P}_7^{\text{out}} \\ \bar{Q}_8^{\text{out}} \end{bmatrix} = \begin{bmatrix} S_{11} & S_{12} & S_{13} & S_{14} & S_{15} & S_{16} & S_{17} & S_{18} \\ S_{21} & S_{22} & S_{23} & S_{24} & S_{25} & S_{26} & S_{27} & S_{28} \\ S_{31} & S_{32} & S_{33} & S_{34} & S_{35} & S_{36} & S_{37} & S_{38} \\ S_{41} & S_{42} & S_{43} & S_{44} & S_{45} & S_{46} & S_{47} & S_{48} \\ S_{51} & S_{52} & S_{53} & S_{54} & S_{55} & S_{56} & S_{57} & S_{58} \\ S_{61} & S_{62} & S_{63} & S_{64} & S_{65} & S_{66} & S_{67} & S_{68} \\ S_{71} & S_{72} & S_{73} & S_{74} & S_{75} & S_{76} & S_{77} & S_{78} \\ S_{81} & S_{82} & S_{83} & S_{84} & S_{85} & S_{86} & S_{87} & S_{88} \end{bmatrix} \begin{bmatrix} \bar{P}_1^{\text{in}} \\ \bar{Q}_2^{\text{in}} \\ \bar{P}_3^{\text{in}} \\ \bar{P}_4^{\text{in}} \\ \bar{P}_5^{\text{in}} \\ \bar{Q}_6^{\text{in}} \\ \bar{P}_7^{\text{in}} \\ \bar{Q}_8^{\text{in}} \end{bmatrix}. \tag{C5}$$

When Eq. (30) in the main text is applied, it implies that Ports 1–4 are excited as only input. No reflection is allowed, which leads to $S_{aa} = 0\,(a = 1, 2, 3, 4)$. Thus, Eq.(C5) can be simplified to

$$\begin{bmatrix} \bar{P}_5^{\text{out}} \\ \bar{Q}_6^{\text{out}} \\ \bar{P}_7^{\text{out}} \\ \bar{Q}_8^{\text{out}} \end{bmatrix} = \begin{bmatrix} S_{15} & S_{16} & S_{17} & S_{18} \\ S_{25} & S_{26} & S_{27} & S_{28} \\ S_{35} & S_{36} & S_{37} & S_{38} \\ S_{45} & S_{46} & S_{47} & S_{48} \end{bmatrix} \begin{bmatrix} \bar{P}_1^{\text{in}} \\ \bar{Q}_2^{\text{in}} \\ \bar{P}_3^{\text{in}} \\ \bar{P}_4^{\text{in}} \end{bmatrix}. \tag{C6}$$

It should be metioned that purely oblique incidence with specific mode is difficult in the simulations with single meta-atom. The excitation setup follows the same procedure as that used for normal incidence, as highlighted in Appendix D in the revised manuscript. To retrieve the scattering matrix, horizontal and vertical Body Loads on a $w_{cell} \times 3$ rectangular area are applied sequentially near the upper and lower PML. This configuration provides four different excitations and ensures sufficient linear independence to establish a system of equations as

$$\begin{bmatrix} \bar{P}_5^{\text{out},1} & \bar{P}_5^{\text{out},2} & \bar{P}_5^{\text{out},2} & \bar{P}_5^{\text{out},4} \\ \bar{Q}_6^{\text{out},1} & \bar{Q}_6^{\text{out},2} & \bar{Q}_6^{\text{out},3} & \bar{Q}_6^{\text{out},4} \\ \bar{P}_7^{\text{out},1} & \bar{P}_7^{\text{out},2} & \bar{P}_7^{\text{out},3} & \bar{P}_7^{\text{out},4} \\ \bar{Q}_8^{\text{out},1} & \bar{Q}_8^{\text{out},2} & \bar{Q}_8^{\text{out},3} & \bar{Q}_8^{\text{out},4} \end{bmatrix} = \begin{bmatrix} S_{15} & S_{16} & S_{17} & S_{18} \\ S_{25} & S_{26} & S_{27} & S_{28} \\ S_{35} & S_{36} & S_{37} & S_{38} \\ S_{45} & S_{46} & S_{47} & S_{48} \end{bmatrix} \begin{bmatrix} \bar{P}_1^{\text{in},1} & \bar{P}_1^{\text{in},2} & \bar{P}_1^{\text{in},3} & \bar{P}_1^{\text{in},4} \\ \bar{Q}_2^{\text{in},1} & \bar{Q}_2^{\text{in},2} & \bar{Q}_2^{\text{in},3} & \bar{Q}_2^{\text{in},4} \\ \bar{P}_3^{\text{in},1} & \bar{P}_3^{\text{in},2} & \bar{P}_3^{\text{in},3} & \bar{P}_3^{\text{in},4} \\ \bar{P}_4^{\text{in},1} & \bar{P}_4^{\text{in},1} & \bar{P}_4^{\text{in},3} & \bar{P}_4^{\text{in},4} \end{bmatrix}. \tag{C7}$$

where the number in the upper corner indicates the number of times it is excited. Then, the scattering matrix can be solved directly.

Appendix D: Numerical simulations

Numerical simulations in Figs. 3, 4 and 6 are conducted with the COMSOL Multiphysics Solid Mechanics module. Normalization is performed on a uniform strip with the same settings as for optimization, but replacing the structure with a uniform background medium. The source is set as Body Load on a $w_{cell} \times 3$ cm rectangular area next to the lower or upper perfect matching layer, whose Force per unit area is $(0, 1)$ for longitudinal wave and $(1, 0)$ for transverse wave. The operating frequency in all simulations is uniformly set to $f_0 = 30$kHz.

The same excitation source settings as for normalization are used for optimization. The sources for optimization of Cases 1, 4 and 5 are two excitations of longitudinal and transverse waves set on the lower side of the meta-atom. The sources for optimization of Cases 2 and 4 are two longitudinal wave excitations set on the upper and lower sides of the meta-atom. The sources for optimization of the meta-atom under oblique incidence are horizontal and vertical Body Loads that are set sequentially to both upper and lower sides of the meta-atom. Therefore, linearly dependent excitations that would prevent the scattering matrix from being fully determined can be avoided as mentioned in Appendix A. The mesh has a maximum size of $\lambda_Q/10$ and a minimum size of $\lambda_Q/15$ for convergence. The discretization uses quadratic Lagrange elements. All settings, including boundary conditions, mesh, excitation and discretization in Figs. 3 are the same as for normalization. The scale factor of the deformation is set to 8×10^7 for observation purposes.

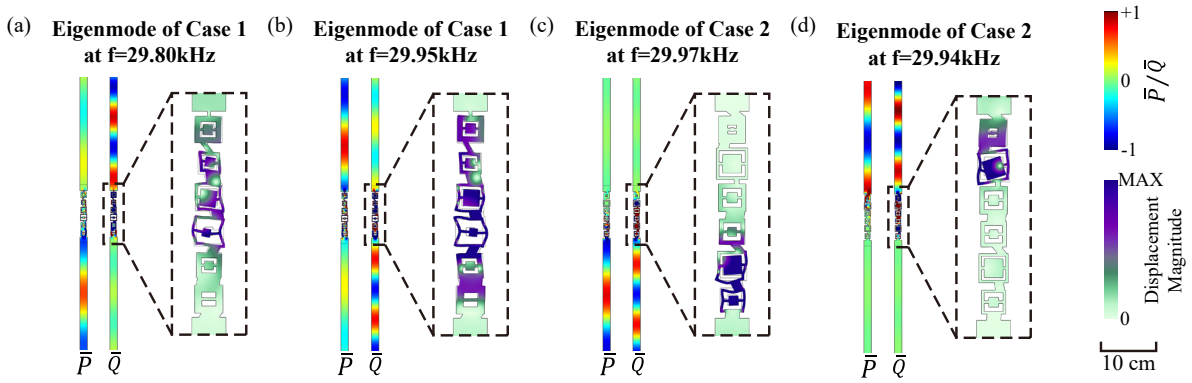

FIG. 8. Eigenmodes of the designed meta-atom. (a) The eigenmode of the meta-atom in Case 1 at 29.80kHz. (b) The eigenmode of the meta-atom in Case 1 at 29.95kHz. (c) The eigenmode of the meta-atom in Case 2 at 29.97kHz. (d) The eigenmode of the meta-atom in Case 2 at 29.94kHz.

Simulations in Fig. 4 are conducted on a 1.2 m × 1.2 m plate under the assumption of plane stress. It is surrounded by a perfect matching layer with a width of 10cm. The metasurface composed of an array of 60 meta-atoms is located in the center of the plate. The excitation source is set as a 50 cm × 3 cm rectangular area 35 cm away from the metasurface in order to match the experiment. A 2 cm × 6 cm slot is set on both sides of the excitation source to guide the propagation of elastic waves. Normalization is performed with the same method as above. The simulation in Fig. 6 involves rotation of the excitation source around the origin by 30.0° for longitudinal waves and 16.8° for transverse waves. The settings for mesh and discretization are the same as those in Figs. 3.

Appendix E: Eigenmodes of the elastic meta-atoms in Cases 1-2

The eigenmodes of the designed meta-atoms are depicted in Fig. 8 to reveal the physical essence of these internal channels. Simulation settings adopt the same mesh and discretization as those in Figs. 3. The perfect matching layer and excitation source are removed. The background medium on both sides is extended to $l_0 = 90\lambda_p$ and both ends are set as Low-Reflecting Boundary (not drawn for simplicity). It can be noted that the eigenmodes in Figs. 8 (a) and (b) are consistent with Figs. 3 (a,d) and (b,c), respectively. The transverse and longitudinal wave fields on both sides of the meta-atom are basically the same. The deformation insider the compression-torsion coupling meta-atom is also similar. The eigenfrequencies corresponding to the two eigenmodes are $f = 29.80$ kHz and $f = 29.95$ kHz, which are close to the operating frequency $f_0 = 30$ kHz. The phenomenon becomes more apparent for the case of reflection as shown in Figs. 8 (c) and (d). Their eigenfrequencies are $f = 29.97$ kHz and $f = 29.94$ kHz, which can be seen as being identical with operating frequency. The eigenmodes are consistent with the vibration mode Figs. 3 (g,h) and (i,j), respectively, as well. It can be concluded that the physical essence of the natural channels inside the meta-atom is two independent modes.

Appendix F: Additional examples for full polarity manipulation

The case of selective transmission is given in Figs. 9(a-e). As shown in Fig. 9(a), one channel connects port 1 to port 3 (yellow channel), but the other channel connecting port 2 to port 4 (orange channel) is broken. The yellow channel should provide complete transmission

$$|S_{13}| = |S_{31}| = 1. \tag{F1}$$

The broken orange channel results in a 100% reflection coefficient

$$|S_{22}| = |S_{44}| = 1. \tag{F2}$$

The amplitudes of each component of its scattering matrix are

$$\mathrm{abs}\,(\mathbf{S}) = \begin{bmatrix} 0 & 0 & 1 & 0 \\ 0 & 1 & 0 & 0 \\ 1 & 0 & 0 & 0 \\ 0 & 0 & 0 & 1 \end{bmatrix}, \tag{F3}$$

The fitness function is defined as

$$f = \min\left\{|S_{13}|, |S_{31}|, |S_{22}|, |S_{44}|\right\}. \tag{F4}$$

The detailed optimization results are recorded in the fourth column of Table I, and the corresponding amplitudes of each component of the scattering matrix are recorded in the forth column of Table II.

The case of unidirectional mode conversion is given in Figs. 9(f-j). As shown in Fig. 9(f), one channel connects port 1 to port 4 (yellow channel), but the other channel connecting port 2 to port 3 (orange channel) is broken. The yellow channel should provide complete transmission

$$|S_{14}| = |S_{41}| = 1. \tag{F5}$$

The broken orange channel results in a 100% reflection coefficient

$$|S_{22}| = |S_{33}| = 1. \tag{F6}$$

The amplitudes of each component of its scattering matrix are

$$\mathrm{abs}\left(\mathbf{S}\right) = \begin{bmatrix} 0 & 0 & 0 & 1 \\ 0 & 1 & 0 & 0 \\ 0 & 0 & 1 & 0 \\ 1 & 0 & 0 & 0 \end{bmatrix}, \tag{F7}$$

The fitness function is defined as

$$f = \min\left\{|S_{14}|, |S_{41}|, |S_{22}|, |S_{33}|\right\}. \tag{F8}$$

The detailed optimization results are recorded in the fifth column of Table I, and the corresponding amplitudes of each component of the scattering matrix are recorded in the fifth column of Table II.

It should be mentioned that this case can not be directly achieved by a medium described by Eq. (13). The longitudinal or transverse waves incident from both sides respond in different forms, which results in directionality that cannot be supported by symmetrical constitutive model. However, due to vertical asymmetry being allowed in the structures as shown in Fig. 1(d), a certain directionality can be introduced. This asymmetry may contribute to Willis coupling[100], leading to the realization of unidirectional mode conversion.

The case of complete transmission is given in Figs. 9(k-o). As shown in Fig. 9(k), one channel connects port 1 to port 3 (yellow channel), and the other channel connects port 2 to port 4 (orange channel). The yellow channel should provide complete transmission

$$|S_{13}| = |S_{31}| = 1. \tag{F9}$$

The transmittance of the orange channel should also be 100%

$$|S_{24}| = |S_{42}| = 1. \tag{F10}$$

The amplitudes of each component of its scattering matrix are

$$\mathrm{abs}\left(\mathbf{S}\right) = \begin{bmatrix} 0 & 0 & 1 & 0 \\ 0 & 0 & 0 & 1 \\ 1 & 0 & 0 & 0 \\ 0 & 1 & 0 & 0 \end{bmatrix}, \tag{F11}$$

THe fitness function is defined as

$$f = \min\left\{|S_{13}|, |S_{31}|, |S_{24}|, |S_{42}|\right\}. \tag{F12}$$

The detailed optimization results is recorded in the fifth column of Table I, and the corresponding amplitudes of each component of the scattering matrix are recorded in the fifth column of Table II.

TABLE I. Optimized parameters [units: cm].

	Case 1	Case 2	Case 3	Case 4	Case 5	Asymmetric meta-atom
w^1	0.12	0.48	0.51	0.54	0.49	0.31
d_u^1	0.01	0.24	-0.065	-0.20	0.05	-0.265
a_o^1	0.51	0.52	0.40	0.51	0.38	0.50
a_i^1	0.30	0.17	0.25	0.41	0.28	0.30
a_m^1	0.20	0.07	0.11	0.22	0.18	0.16
d_d^1	-0.19	-0.275	0.00	0.16	0.14	-0.045
w^2	0.21	0.41	0.64	0.36	0.40	0.75
d_u^2	0.05	-0.33	0.14	-0.18	0.24	-0.125
a_o^2	0.41	0.60	0.54	0.40	0.48	0.58
a_i^2	0.29	0.50	0.31	0.30	0.38	0.47
a_m^2	0.19	0.36	0.21	0.07	0.28	0.20
d_d^2	0.09	0.17	-0.13	-0.07	0.015	-0.05
w^3	0.56	0.19	0.66	0.58	0.85	-0.90
d_u^3	0.20	0.17	0.13	-0.11	-0.035	0.00
a_o^3	0.52	0.53	0.54	0.44	0.50	0.53
a_i^3	0.42	0.36	0.42	0.34	0.40	0.43
a_m^3	0.32	0.20	0.32	0.21	0.30	0.26
d_d^3	0.25	0.135	0.10	-0.09	0.00	0.10
w^4	0.46	0.71	0.80	0.62	0.92	0.70
d_u^4	0.30	0.095	-0.04	-0.13	-0.05	0.00
a_o^4	0.57	0.49	0.52	0.48	0.55	0.43
a_i^4	0.47	0.34	0.42	0.22	0.40	0.33
a_m^4	0.16	0.17	0.32	0.12	0.29	0.23
d_d^4	0.22	0.12	0.305	0.10	0.01	0.00
w^5	0.42	0.35	0.27	0.64	0.80	0.70
d_u^5	0.09	0.33	0.295	-0.22	0.04	-0.14
a_o^5	0.48	0.56	0.51	0.58	0.48	0.57
a_i^5	0.29	0.46	0.30	0.48	0.38	0.47
a_m^5	0.17	0.36	0.20	0.38	0.28	0.37
d_d^5	0.00	0.20	0.215	-0.12	-0.03	-0.17
w^6	0.88	0.35	0.43	0.54	0.82	0.63
d_u^6	-0.03	0.245	-0.02	-0.13	0.00	-0.10
a_o^6	0.54	0.46	0.58	0.56	0.45	0.50
a_i^6	0.27	0.36	0.35	0.32	0.35	0.21
a_m^6	0.05	0.19	0.25	0.09	0.25	0.11
d_d^6	0.11	0.02	0.23	-0.06	0.09	-0.305
w^7	0.78	0.54	0.54	0.92	1.00	0.23

TABLE II. Amplitude of optimized scattering matrix.

	Case 1	Case 2	Case 3
abs($\mathbf{S}$)	$\begin{bmatrix} 0.12 & 0.16 & 0.19 & 0.97 \\ 0.16 & 0.05 & 0.95 & 0.21 \\ 0.19 & 0.95 & 0.11 & 0.16 \\ 0.97 & 0.21 & 0.16 & 0.05 \end{bmatrix}$	$\begin{bmatrix} 0.12 & 0.99 & 0.04 & 0.04 \\ 0.99 & 0.12 & 0.04 & 0.03 \\ 0.04 & 0.04 & 0.09 & 0.99 \\ 0.01 & 0.03 & 0.99 & 0.09 \end{bmatrix}$	$\begin{bmatrix} 0.09 & 0.08 & 0.99 & 0.07 \\ 0.08 & 0.99 & 0.08 & 0.03 \\ 0.99 & 0.08 & 0.09 & 0.07 \\ 0.07 & 0.03 & 0.07 & 0.99 \end{bmatrix}$

Appendix G: Experiments

The experimental sample is a rectangular 6061 aluminum alloy plate 1.2 m × 1.2 m ×1 mm with a mass density of 2700 kg/m^3, plane stress longitudinal wave modulus of 77 GPa, and plane stress transverse wave modulus of 26 GPa, which is fabricated by laser cutting. All geometries are set to be consistent with the simulation, except that the perfect matching layers are replaced with blue tack to avoid boundary reflections affecting observation. The sample is suspended vertically on an aluminum frame. Signals generated and collected in the experiment are controlled by Polytec controller connected to a computer. The source is selected as a 3-cycle sinusoidal burst signal at 30kHz,

TABLE III. Amplitude of optimized scattering matrix.

	Case 4	Case 5	Asymmetric meta-atom
$abs(\mathbf{S})$	$\begin{bmatrix} 0.07 & 0.19 & 0.20 & 0.96 \\ 0.19 & 0.96 & 0.04 & 0.20 \\ 0.20 & 0.04 & 0.96 & 0.20 \\ 0.96 & 0.20 & 0.20 & 0.03 \end{bmatrix}$	$\begin{bmatrix} 0.17 & 0.96 & 0.16 & 0.14 \\ 0.96 & 0.13 & 0.15 & 0.17 \\ 0.15 & 0.15 & 0.19 & 0.96 \\ 0.13 & 0.17 & 0.96 & 0.18 \end{bmatrix}$	$\begin{bmatrix} 0.00 & 0.00 & 0.00 & 0.00 & 0.19 & 0.38 & 0.09 & 0.90 \\ 0.00 & 0.00 & 0.00 & 0.00 & 0.33 & 0.22 & 0.91 & 0.08 \\ 0.00 & 0.00 & 0.00 & 0.00 & 0.83 & 0.40 & 0.28 & 0.28 \\ 0.00 & 0.00 & 0.00 & 0.00 & 0.40 & 0.81 & 0.28 & 0.32 \\ 0.19 & 0.33 & 0.83 & 0.40 & 0.00 & 0.00 & 0.00 & 0.00 \\ 0.38 & 0.22 & 0.40 & 0.81 & 0.00 & 0.00 & 0.00 & 0.00 \\ 0.09 & 0.91 & 0.28 & 0.28 & 0.00 & 0.00 & 0.00 & 0.00 \\ 0.90 & 0.08 & 0.27 & 0.32 & 0.00 & 0.00 & 0.00 & 0.00 \end{bmatrix}$

which is excited by 8 pairs of 6cm ×3 cm piezoelectric transducers symmetrically attached to the front and back of the sample. For the transmission symmetric mode conversion, the measurement area in Fig. 7 (a) consists of two 50cm × 20 cm rectangles located 5 cm above and below the metasurface. Their central axis coincide with the central axis of the metasurface. For asymmetric mode conversion, the measurement area is shifted 5 cm to the right as shown in Fig. 7 (f). There are 77 × 31 evenly distributed points in the measurement area for sampling with a sampling frequency of 1000 kHz. Normalization refers to the maximum value when the incident wave appears completely at the first time in the measurement area.

[1] H. Nassar, B. Yousefzadeh, R. Fleury, M. Ruzzene, A. Alù, C. Daraio, A. N. Norris, G. Huang, M. R. Haberman, Nonreciprocity in acoustic and elastic materials, Nature Reviews Materials 5 (9) (2020) 667–685.

[2] A.-L. Chen, Y.-S. Wang, Y.-F. Wang, H.-T. Zhou, S.-M. Yuan, Design of acoustic/elastic phase gradient metasurfaces: principles, functional elements, tunability, and coding, Applied Mechanics Reviews 74 (2) (2022) 020801.

[3] Y. Zhang, J. Zhao, Y. Huang, C. Yang, W. Yuan, Z. Zhong, J. Ren, Y. Pan, Elastic wave spin and unidirectional routing in thin rod systems, International Journal of Mechanical Sciences 277 (2024) 109512.

[4] W. Yuan, C. Yang, D. Zhang, Y. Long, Y. Pan, Z. Zhong, H. Chen, J. Zhao, J. Ren, Observation of elastic spin with chiral meta-sources, Nature communications 12 (1) (2021) 6954.

[5] K. Y. Bliokh, Elastic spin and orbital angular momenta, Physical Review Letters 129 (20) (2022) 204303.

[6] G. J. Chaplain, J. M. De Ponti, T. A. Starkey, Elastic orbital angular momentum transfer from an elastic pipe to a fluid, Communications Physics 5 (1) (2022) 279.

[7] L. Cao, Y. Zhu, Y. Xu, S.-W. Fan, Z. Yang, B. Assouar, Elastic bound state in the continuum with perfect mode conversion, Journal of the Mechanics and Physics of Solids 154 (2021) 104502. doi:https://doi.org/10.1016/j.jmps.2021.104502.
URL https://www.sciencedirect.com/science/article/pii/S0022509621001708

[8] C. Piao, S. H. Kim, J. K. Lee, W. G. Choi, Y. Y. Kim, Non-invasive ultrasonic inspection of sludge accumulation in a pipe, Ultrasonics 119 (2022) 106602. doi:https://doi.org/10.1016/j.ultras.2021.106602.
URL https://www.sciencedirect.com/science/article/pii/S0041624X21002225

[9] W. Xu, Y. Zheng, Y. Jiang, Z. Zhang, S. Ma, Y. Cao, Shear wave imaging the active constitutive parameters of living muscles, Acta Biomaterialia 166 (2023) 400–408. doi:https://doi.org/10.1016/j.actbio.2023.05.035.
URL https://www.sciencedirect.com/science/article/pii/S1742706123002908

[10] M. Mitra, S. Gopalakrishnan, Guided wave based structural health monitoring: A review, Smart Materials and Structures 25 (5) (2016) 053001. doi:10.1088/0964-1726/25/5/053001.
URL https://dx.doi.org/10.1088/0964-1726/25/5/053001

[11] F. Ricci, E. Monaco, N. Boffa, L. Maio, V. Memmolo, Guided waves for structural health monitoring in composites: A review and implementation strategies, Progress in Aerospace Sciences 129 (2022) 100790, impact induced dynamic response and failure behavior of aircraft structures. doi:https://doi.org/10.1016/j.paerosci.2021.100790.
URL https://www.sciencedirect.com/science/article/pii/S0376042121000920

[12] P. Cawley, Guided waves in long range nondestructive testing and structural health monitoring: Principles, history of applications and prospects, Non-Destructive Testing and Evaluation International 142 (2024) 103026. doi:https://doi.org/10.1016/j.ndteint.2023.103026.
URL https://www.sciencedirect.com/science/article/pii/S0963869523002414

[13] S. N. Sharma, Y. Lee, Monitoring homeostasis with ultrasound, Science 383 (6687) (2024) 1058–1059. doi:10.1126/science.ado2145.
URL https://www.science.org/doi/abs/10.1126/science.ado2145

[14] J. Liu, N. Liu, Y. Xu, M. Wu, H. Zhang, Y. Wang, Y. Yan, A. Hill, R. Song, Z. Xu, M. Park, Y. Wu, J. L. Ciatti, J. Gu, H. Luan, Y. Zhang, T. Yang, H.-Y. Ahn, S. Li, W. Z. Ray, C. K. Franz, M. R. MacEwan, Y. Huang, C. W. Hammill, H. Wang, J. A. Rogers, Bioresorbable shape-adaptive structures for ultrasonic monitoring of deep-tissue homeostasis,

Science 383 (6687) (2024) 1096–1103. arXiv:https://www.science.org/doi/pdf/10.1126/science.adk9880, doi:10.1126/science.adk9880.
URL https://www.science.org/doi/abs/10.1126/science.adk9880

[15] H.-C. Liu, Y. Zeng, C. Gong, X. Chen, P. Kijanka, J. Zhang, Y. Genyk, H. Tchelepi, C. Wang, Q. Zhou, X. Zhao, Wearable bioadhesive ultrasound shear wave elastography, Science Advances 10 (6) (2024) eadk8426. arXiv:https://www.science.org/doi/pdf/10.1126/sciadv.adk8426, doi:10.1126/sciadv.adk8426.
URL https://www.science.org/doi/abs/10.1126/sciadv.adk8426

[16] W. Xu, Y. Zheng, Z. Yin, Y. Jiang, Z. Zhang, S. Ma, Y. Cao, Imaging the intramuscular pressure of living muscles with shear waves, Journal of the Mechanics and Physics of Solids 192 (2024) 105834. doi:https://doi.org/10.1016/j.jmps.2024.105834.
URL https://www.sciencedirect.com/science/article/pii/S0022509624003004

[17] Y. Jiang, S. Ma, Y. Cao, Guided wave elastography of jugular veins: Theory, method and in vivo experiment, Journal of Biomechanics 160 (2023) 111828. doi:https://doi.org/10.1016/j.jbiomech.2023.111828.
URL https://www.sciencedirect.com/science/article/pii/S0021929023003998

[18] Z. Zhang, G. Y. Li, Y. Jiang, Y. Zheng, A. Gower, M. Destrade, Y. Cao, Noninvasive measurement of local stress inside soft materials with programmed shear waves, Science Advances 9 (2023).

[19] Y.-F. Wang, Y.-Z. Wang, B. Wu, W. Chen, Y.-S. Wang, Tunable and active phononic crystals and metamaterials, Applied Mechanics Reviews 72 (4) (2020) 040801.

[20] M. Kadic, G. W. Milton, M. Van Hecke, M. Wegener, 3d metamaterials, Nature reviews physics 1 (3) (2019) 198–210.

[21] B. Assouar, B. Liang, Y. Wu, Y. Li, J.-C. Cheng, Y. Jing, Acoustic metasurfaces, Nature Reviews Materials 3 (12) (2018) 460–472.

[22] R. Martínez-Sala, J. Sancho, J. V. Sánchez, V. Gómez, J. Llinares, F. Meseguer, et al., Sound attenuation by sculpture, nature 378 (6554) (1995) 241.

[23] R. Zhu, X. Liu, G. Hu, C.-T. Sun, G. Huang, Negative refraction of elastic waves at the deep-subwavelength scale in a single-phase metamaterial, Nature communications 5 (1) (2014) 5510.

[24] T. Guo, X. Yang, Q. Geng, Z. Li, Y. Li, X. Wang, H. Zhang, Anisotropic phononic crystal structure with low-frequency bandgap and heat flux manipulation, Science China Physics, Mechanics & Astronomy 63 (2) (2020) 224711.

[25] Y. Cheng, X. Zhou, G. Hu, Broadband dual-anisotropic solid metamaterials, Scientific reports 7 (1) (2017) 13197.

[26] J. Park, D. Lee, J. Rho, Recent advances in non-traditional elastic wave manipulation by macroscopic artificial structures, Applied Sciences 10 (2) (2020) 547.

[27] J. B. Pendry, D. Schurig, D. R. Smith, Controlling electromagnetic fields, science 312 (5781) (2006) 1780–1782.

[28] S. A. Cummer, D. Schurig, One path to acoustic cloaking, New journal of physics 9 (3) (2007) 45–45.

[29] A. N. Norris, Acoustic cloaking theory, Proceedings of the Royal Society A: Mathematical, Physical and Engineering Sciences 464 (2097) (2008) 2411–2434.

[30] M. Farhat, S. Enoch, S. Guenneau, A. Movchan, Broadband cylindrical acoustic cloak for linear surface waves in a fluid, Physical review letters 101 (13) (2008) 134501.

[31] S. A. Cummer, B.-I. Popa, D. Schurig, D. R. Smith, J. Pendry, M. Rahm, A. Starr, Scattering theory derivation of a 3d acoustic cloaking shell, Physical review letters 100 (2) (2008) 024301.

[32] U. Iemma, Theoretical and numerical modeling of acoustic metamaterials for aeroacoustic applications, Aerospace 3 (2) (2016) 15.

[33] N. Yu, P. Genevet, M. A. Kats, F. Aieta, J.-P. Tetienne, F. Capasso, Z. Gaburro, Light propagation with phase discontinuities: generalized laws of reflection and refraction, science 334 (6054) (2011) 333–337.

[34] Y. Xie, W. Wang, H. Chen, A. Konneker, B.-I. Popa, S. A. Cummer, Wavefront modulation and subwavelength diffractive acoustics with an acoustic metasurface, Nature communications 5 (1) (2014) 5553.

[35] Y.-Z. Tian, R. Li, Y.-F. Wang, V. Laude, Y.-S. Wang, Transmedia transmission enhancement based on transformation acoustics, Phys. Rev. B 110 (21) (2024) 214101.

[36] H.-T. Zhou, S.-C. Zhang, T. Zhu, Y.-Z. Tian, Y.-F. Wang, Y.-S. Wang, Hybrid metasurfaces for perfect transmission and customized manipulation of sound across water–air interface, Advanced Science 10 (19) (2023) 2207181.

[37] C.-Y. Li, H.-T. Zhou, X.-S. Li, Y.-F. Wang, Y.-S. Wang, Janus metasurface for underwater sound manipulation, Advanced Functional Materials 34 (42) (2024) 2408572.

[38] X.-S. Li, H.-T. Zhou, Y.-F. Wang, Y.-S. Wang, Modulation of acoustic self-accelerating beams with tunable curved metasurfaces, Applied Physics Letters 118 (2) (2021).

[39] D. Torrent, Acoustic anomalous reflectors based on diffraction grating engineering, Physical Review B 98 (6) (2018) 060101.

[40] Z. Hou, X. Fang, Y. Li, B. Assouar, Highly efficient acoustic metagrating with strongly coupled surface grooves, Physical Review Applied 12 (3) (2019) 034021.

[41] C.-Y. Li, H.-T. Zhou, Y.-F. Wang, Y.-S. Wang, Shallow-water waveguide with hybrid boundaries for underwater acoustic metamaterial measurements, Physical Review Applied 24 (5) (2025) 054074.

[42] B. Xie, K. Tang, H. Cheng, Z. Liu, S. Chen, J. Tian, Coding acoustic metasurfaces, Advanced Materials 29 (6) (2017) 1603507.

[43] A. Díaz-Rubio, S. A. Tretyakov, Acoustic metasurfaces for scattering-free anomalous reflection and refraction, Physical Review B 96 (12) (2017) 125409.

[44] J. Li, A. Song, S. A. Cummer, Bianisotropic acoustic metasurface for surface-wave-enhanced wavefront transformation, Physical Review Applied 14 (4) (2020) 044012.

[45] L. Quan, A. Alu, Passive acoustic metasurface with unitary reflection based on nonlocality, Physical Review Applied 11 (5) (2019) 054077.

[46] X. Peng, J. Li, C. Shen, S. A. Cummer, Efficient scattering-free wavefront transformation with power flow conformal bianisotropic acoustic metasurfaces, Applied Physics Letters 118 (6) (2021).

[47] J. Li, A. Díaz-Rubio, C. Shen, Z. Jia, S. Tretyakov, S. Cummer, Highly efficient generation of angular momentum with cylindrical bianisotropic metasurfaces, Physical Review Applied 11 (2) (2019) 024016.

[48] Y.-Z. Tian, Y.-F. Wang, V. Laude, Y.-S. Wang, Generalized acoustic impedance metasurface, Communications Physics 7 (1) (2024) 34.

[49] Y. Liu, Z. Liang, F. Liu, O. Diba, A. Lamb, J. Li, Source illusion devices for flexural lamb waves using elastic metasurfaces, Physical review letters 119 (3) (2017) 034301.

[50] Y. Chen, M. Zheng, X. Liu, Y. Bi, Z. Sun, P. Xiang, J. Yang, G. Hu, Broadband solid cloak for underwater acoustics, Physical Review B 95 (18) (2017) 180104.

[51] Y. Chen, X. Liu, G. Hu, Latticed pentamode acoustic cloak, Scientific reports 5 (1) (2015) 15745.

[52] P. A. Kerrian, A. D. Hanford, D. E. Capone, B. S. Beck, Development of a perforated plate underwater acoustic ground cloak, The Journal of the Acoustical Society of America 146 (4) (2019) 2303–2308.

[53] J.-j. Liu, B. Liang, J.-c. Cheng, Focusing a two-dimensional acoustic vortex beyond diffraction limit on an ultrathin structured surface, Physical Review Applied 15 (1) (2021) 014015.

[54] X.-L. Tang, Y.-D. Liu, X.-Q. Zhang, Y. Liu, T.-X. Ma, M. Kim, Y.-S. Wang, Broadband acoustic energy harvesting via topological edge and bulk states in phononic cavity chains, Physical Review Applied 24 (4) (2025) 044048.

[55] X.-L. Tang, X.-Q. Zhang, T.-X. Ma, M. Kim, Y.-S. Wang, Topological rainbow trapping and broadband piezoelectric energy harvesting of acoustic waves in gradient phononic crystals with coupled interfaces, Applied Acoustics 233 (2025) 110630.

[56] Y. Chen, L. Fan, J. Zhu, L. An, Z. Su, Rainbow energy harvesting using a high-order topological meta-device, Nano Energy 127 (2024) 109722.

[57] H. Xiao, T. Tan, T. Li, L. Zhang, C. Yuan, Z. Yan, Enhanced multi-band acoustic energy harvesting using double defect modes of helmholtz resonant metamaterial, Smart Materials and Structures 32 (10) (2023) 105030.

[58] Y.-Z. Tian, X.-L. Tang, Y.-F. Wang, V. Laude, Y.-S. Wang, Annular acoustic impedance metasurfaces for encrypted information storage, Phys. Rev. Appl. 20 (2023) 044053. doi:10.1103/PhysRevApplied.20.044053.
URL https://link.aps.org/doi/10.1103/PhysRevApplied.20.044053

[59] X. Fang, X. Wang, Y. Li, Acoustic splitting and bending with compact coding metasurfaces, Physical Review Applied 11 (6) (2019) 064033.

[60] S. Gao, Y. Li, C. Ma, Y. Cheng, X. Liu, Emitting long-distance spiral airborne sound using low-profile planar acoustic antenna, Nature Communications 12 (1) (2021) 2006.

[61] Z. Sun, Y. Shi, X. Sun, H. Jia, Z. Jin, K. Deng, J. Yang, Underwater acoustic multiplexing communication by pentamode metasurface, Journal of Physics D: Applied Physics 54 (20) (2021) 205303.

[62] C. Shi, M. Dubois, Y. Wang, X. Zhang, High-speed acoustic communication by multiplexing orbital angular momentum, Proceedings of the National Academy of Sciences 114 (28) (2017) 7250–7253.

[63] L. Shi, T. Zhu, Y.-L. Du, H.-T. Zhou, Y.-Z. Tian, Y.-F. Wang, Y.-S. Wang, A two-dimensional discrete metasurface for wireless acoustic communication through water–air interface, Engineering Structures 341 (2025) 120611.

[64] Y. Zhu, N. J. Gerard, X. Xia, G. C. Stevenson, L. Cao, S. Fan, C. M. Spadaccini, Y. Jing, B. Assouar, Systematic design and experimental demonstration of transmission-type multiplexed acoustic metaholograms, Advanced Functional Materials 31 (27) (2021) 2101947.

[65] J. Zhang, Y. Tian, Y. Cheng, X. Liu, Acoustic holography using composite metasurfaces, Applied Physics Letters 116 (3) (2020).

[66] M. Xu, W. S. Harley, Z. Ma, P. V. Lee, D. J. Collins, Sound-speed modifying acoustic metasurfaces for acoustic holography, Advanced Materials 35 (14) (2023) 2208002.

[67] R. Burstow, D. Andrés, N. Jiménez, F. Camarena, M. Thanou, A. N. Pouliopoulos, Acoustic holography in biomedical applications, Physics in Medicine & Biology 70 (6) (2025) 06TR01.

[68] M. Xu, J. Wang, W. S. Harley, P. V. Lee, D. J. Collins, Programmable acoustic holography using medium-sound-speed modulation, Advanced Science 10 (23) (2023) 2301489.

[69] H.-W. Dong, C. Shen, Z. Liu, S.-D. Zhao, Z. Ren, C.-X. Liu, X. He, S. A. Cummer, Y.-S. Wang, D. Fang, et al., Inverse design of phononic meta-structured materials, Materials Today (2024).

[70] G. W. Milton, M. Briane, J. R. Willis, On cloaking for elasticity and physical equations with a transformation invariant form, New journal of physics 8 (10) (2006) 248–248.

[71] A. N. Norris, A. L. Shuvalov, Elastic cloaking theory, Wave Motion 48 (6) (2011) 525–538.

[72] A. Diatta, M. Kadic, M. Wegener, S. Guenneau, Scattering problems in elastodynamics, Physical review B 94 (10) (2016) 100105.

[73] H.-T. Zhou, W.-X. Fu, Y.-F. Wang, Y.-S. Wang, V. Laude, C. Zhang, Ultra-broadband passive acoustic metasurface for wide-angle carpet cloaking, Materials & Design 199 (2021) 109414.

[74] H. Zhang, X. Liu, G. Hu, An asymmetric elastic metamaterial model for elastic wave cloaking, Journal of the Mechanics and Physics of Solids 135 (2020) 103796.

[75] Y.-Z. Tian, Y.-F. Wang, G.-Y. Huang, V. Laude, Y.-S. Wang, Dual-function thermoelastic cloak based on coordinate transformation theory, International Journal of Heat and Mass Transfer 195 (2022) 123128. doi:https://doi.org/10.1016/j.ijheatmasstransfer.2022.123128.

URL https://www.sciencedirect.com/science/article/pii/S0017931022005993
[76] Y.-C. Su, T. Chen, L.-H. Ko, M.-H. Lu, Design of metasurfaces to enable shear horizontal wave trapping, Journal of Applied Physics 128 (17) (2020).
[77] C. Sun, A. Song, S. Peng, Y. Xiang, Dynamic geometric phase mechanism for multi-mode guided wave manipulation, International Journal of Mechanical Sciences (2025) 110043.
[78] S. Y. Kim, W. Lee, J. S. Lee, Y. Y. Kim, Longitudinal wave steering using beam-type elastic metagratings, Mechanical Systems and Signal Processing 156 (2021) 107688.
[79] M. Jiang, H.-T. Zhou, T. Zhu, Y.-F. Wang, B. Assouar, Y.-S. Wang, Impedance theory-based elastic metasurface enabling precise mode conversion and preservation, Journal of the Mechanics and Physics of Solids 203 (2025) 106231. doi:https://doi.org/10.1016/j.jmps.2025.106231.
URL https://www.sciencedirect.com/science/article/pii/S0022509625002078
[80] Y. Bobrovnitskii, Impedance theory of wave propagation on infinite periodic structures, Journal of Sound and Vibration 525 (2022) 116801.
[81] H. J. Lee, J.-R. Lee, S. H. Moon, T.-J. Je, E.-c. Jeon, K. Kim, Y. Y. Kim, Off-centered double-slit metamaterial for elastic wave polarization anomaly, Scientific reports 7 (1) (2017) 15378.
[82] B. Ahn, H. J. Lee, Y. Y. Kim, Topology optimization of anisotropic metamaterials tracing the target efc and field polarization, Computer Methods in Applied Mechanics and Engineering 333 (2018) 176–196.
[83] M. S. Kim, W. R. Lee, Y. Y. Kim, J. H. Oh, Transmodal elastic metasurface for broad angle total mode conversion, Applied Physics Letters 112 (24) (2018).
[84] S. W. Lee, H. M. Seung, W. Choi, M. Kim, J. H. Oh, Broad-angle refractive transmodal elastic metasurface, Applied Physics Letters 117 (21) (2020).
[85] X. Su, Z. Lu, A. N. Norris, Elastic metasurfaces for splitting sv-and p-waves in elastic solids, Journal of Applied Physics 123 (9) (2018).
[86] J. Mei, L. Fan, X. Hong, Elastic metagratings with simultaneous highly efficient control over longitudinal and transverse waves for multiple functionalities, Physical Review Applied 18 (1) (2022) 014002.
[87] S. W. Lee, S. I. Kim, H. M. Seung, J. H. Oh, Mode-selective elastic metasurfaces, Physical Review Applied 19 (1) (2023) 014024.
[88] M. Zheng, X. Liu, Y. Chen, H. Miao, R. Zhu, G. Hu, Theory and realization of nonresonant anisotropic singly polarized solids carrying only shear waves, Physical Review Applied 12 (1) (2019) 014027.
[89] X. Yang, S. Yao, Y. Chai, Y. Li, Efficient pure-mode elastic mode-converting diode, Journal of Physics D: Applied Physics 54 (36) (2021) 365302.
[90] Y. Chai, S. Yao, X. Yang, Y. Li, Asymmetric full mode-converting transmission of elastic waves, New Journal of Physics 25 (5) (2023) 053027.
[91] X. Yang, Y. Y. Kim, Asymptotic theory of bimodal quarter-wave impedance matching for full mode-converting transmission, Physical Review B 98 (14) (2018) 144110.
[92] W. Lee, J. Lee, C. I. Park, Y. Y. Kim, Polarization-independent full mode-converting elastic metasurfaces, International Journal of Mechanical Sciences 266 (2024) 108975.
[93] H.-T. Zhou, M. Jiang, J.-H. Zhu, Y. Li, Q. Li, Y.-F. Wang, C.-W. Qiu, Y.-S. Wang, Underwater scattering exceptional point by metasurface with fluid-solid interaction, Advanced Functional Materials 34 (37) (2024) 2404282.
[94] M. Brun, S. Guenneau, A. B. Movchan, Achieving control of in-plane elastic waves, Applied physics letters 94 (6) (2009).
[95] Y.-Z. Tian, Z.-R. Wei, Y.-F. Wang, V. Laude, Y.-S. Wang, Adjustable phase-amplitude-phase acoustic metasurface for the implementation of arbitrary impedance matrices, Research 7 (2024) 0502.
[96] D. M. Pozar, Microwave engineering: theory and techniques, John wiley & sons, 2021.
[97] J. Li, C. Shen, A. Díaz-Rubio, S. A. Tretyakov, S. A. Cummer, Systematic design and experimental demonstration of bianisotropic metasurfaces for scattering-free manipulation of acoustic wavefronts, Nature communications 9 (1) (2018) 1342.
[98] X. Su, A. N. Norris, Focusing, refraction, and asymmetric transmission of elastic waves in solid metamaterials with aligned parallel gaps, The Journal of the Acoustical Society of America 139 (6) (2016) 3386–3394.
[99] Y. Liu, H. Li, J. Zhang, X. Liu, L. Wu, H. Ning, N. Hu, Design of elastic metasurfaces for controlling shear vertical waves using uniaxial scaling transformation method, International Journal of Mechanical Sciences 169 (2020) 105335.
[100] C. F. Sieck, A. Alù, M. R. Haberman, Origins of willis coupling and acoustic bianisotropy in acoustic metamaterials through source-driven homogenization, Physical Review B 96 (10) (2017) 104303.
[101] H. Nassar, X. Xu, A. Norris, G. Huang, Modulated phononic crystals: Non-reciprocal wave propagation and willis materials, Journal of the Mechanics and Physics of Solids 101 (2017) 10–29.
[102] Y. Liu, Z. Liang, J. Zhu, L. Xia, O. Mondain-Monval, T. Brunet, A. Alù, J. Li, Willis metamaterial on a structured beam, Physical Review X 9 (1) (2019) 011040.

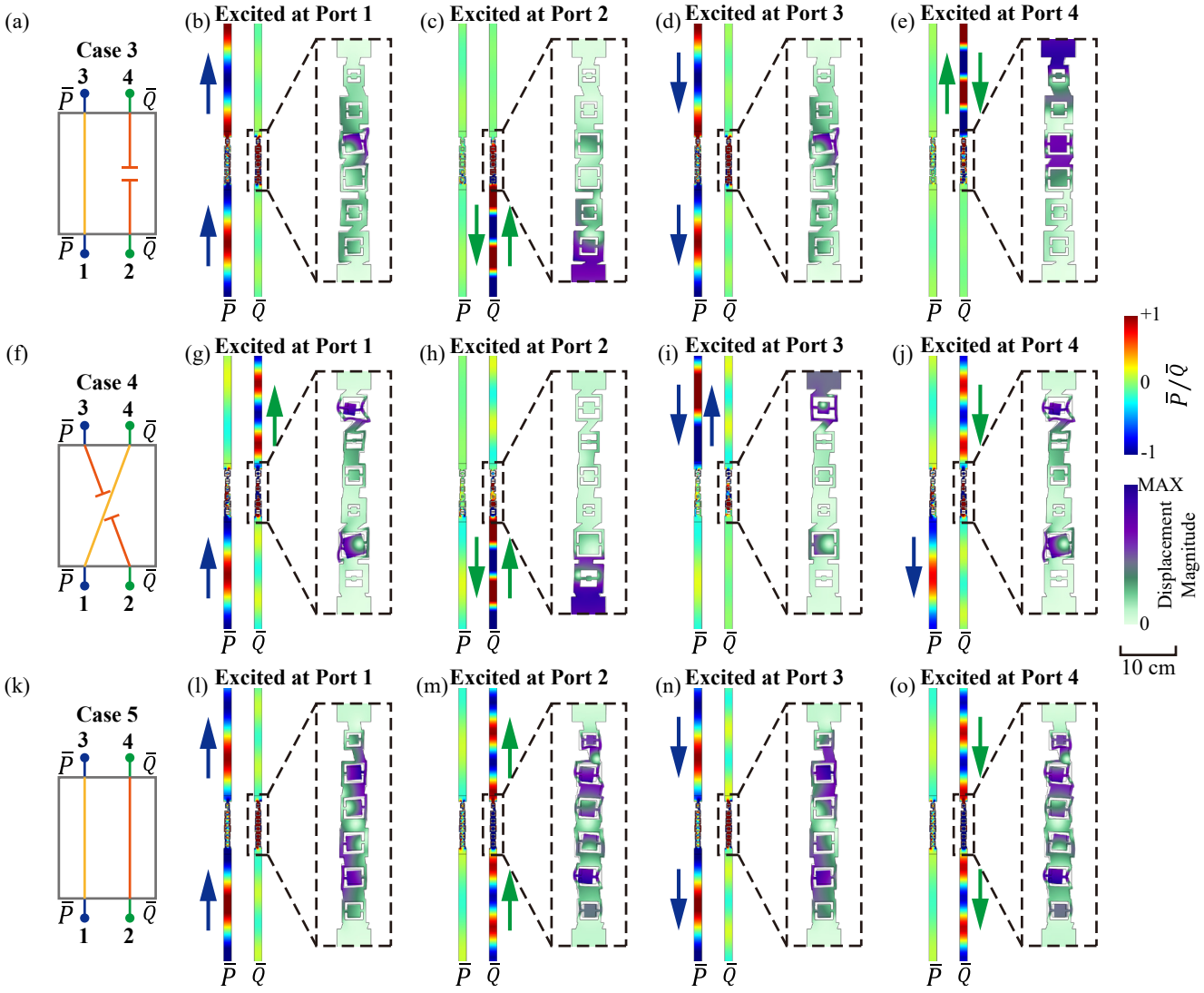

FIG. 9. The structure design and responses for selective transmission (Case 3), unidirectional mode conversion (Case 4), and complete transmission (Case 5). (a) 4-port model for selective transmission. (b) The response of selective transmission meta-atom under a longitudinal wave incident from the lower side, i.e. excited at port 1. (c) The response of selective transmission meta-atom under a transverse wave incident from the lower side, i.e. excited at port 2. (d) The response of selective transmission meta-atom under a longitudinal wave incident from the upper side, i.e. excited at port 3. (e) The response of selective transmission meta-atom under a transverse wave incident from the upper side, i.e. excited at port 4. (f) 4-port model for unidirectional mode conversion. (g) The response of unidirectional mode conversion meta-atom under a longitudinal wave incident from the lower side, i.e. excited at port 1. (h) The response of unidirectional mode conversion meta-atom under a transverse wave incident from the lower side, i.e. excited at port 2. (i) The response of unidirectional mode conversion meta-atom under a longitudinal wave incident from the upper side, i.e. excited at port 3. (j) The response of unidirectional mode conversion meta-atom under a transverse wave incident from the upper side, i.e. excited at port 4. (k) 4-port model for complete transmission. (l) The response of complete transmission meta-atom under a longitudinal wave incident from the lower side, i.e. excited at port 1. (m) The response of complete transmission meta-atom under a transverse wave incident from the lower side, i.e. excited at port 2. (n) The response of complete transmission meta-atom under a longitudinal wave incident from the upper side, i.e. excited at port 3. (o) The response of complete transmission meta-atom under a transverse wave incident from the upper side, i.e. excited at port 4.